

# Measurement of neutron production in atmospheric neutrino interactions at Super-Kamiokande

S. Han,<sup>2</sup> K. Abe,<sup>1,48</sup> C. Bronner,<sup>1</sup> Y. Hayato,<sup>1,48</sup> K. Hiraide,<sup>1,48</sup> K. Hosokawa,<sup>1</sup> K. Ieki,<sup>1,48</sup> M. Ikeda,<sup>1,48</sup> J. Kameda,<sup>1,48</sup> Y. Kanemura,<sup>1</sup> R. Kaneshima,<sup>1</sup> Y. Kashiwagi,<sup>1</sup> Y. Kataoka,<sup>1,48</sup> S. Miki,<sup>1</sup> S. Mine,<sup>1,6</sup> M. Miura,<sup>1,48</sup> S. Moriyama,<sup>1,48</sup> M. Nakahata,<sup>1,48</sup> Y. Nakano,<sup>1</sup> S. Nakayama,<sup>1,48</sup> Y. Noguchi,<sup>1</sup> K. Sato,<sup>1</sup> H. Sekiya,<sup>1,48</sup> H. Shiba,<sup>1</sup> K. Shimizu,<sup>1</sup> M. Shiozawa,<sup>1,48</sup> Y. Sonoda,<sup>1</sup> Y. Suzuki,<sup>1</sup> A. Takeda,<sup>1,48</sup> Y. Takemoto,<sup>1,48</sup> H. Tanaka,<sup>1,48</sup> T. Yano,<sup>1</sup> T. Kajita,<sup>2,48,22</sup> K. Okumura,<sup>2,48</sup> T. Tashiro,<sup>2</sup> T. Tomiya,<sup>2</sup> X. Wang,<sup>2</sup> S. Yoshida,<sup>2</sup> P. Fernandez,<sup>3</sup> L. Labarga,<sup>3</sup> N. Ospina,<sup>3</sup> B. Zaldivar,<sup>3</sup> B. W. Pointon,<sup>5,51</sup> E. Kearns,<sup>4,48</sup> J. L. Raaf,<sup>4</sup> L. Wan,<sup>4</sup> T. Wester,<sup>4</sup> J. Bian,<sup>6</sup> N. J. Grishevich,<sup>6</sup> M. B. Smy,<sup>6,48</sup> H. W. Sobel,<sup>6,48</sup> V. Takhistov,<sup>6,24</sup> A. Yankelevich,<sup>6</sup> J. Hill,<sup>7</sup> M. C. Jang,<sup>8</sup> S. H. Lee,<sup>8</sup> D. H. Moon,<sup>8</sup> R. G. Park,<sup>8</sup> B. Bodur,<sup>9</sup> K. Scholberg,<sup>9,48</sup> C. W. Walter,<sup>9,48</sup> A. Beauchêne,<sup>10</sup> O. Drapier,<sup>10</sup> A. Giampaolo,<sup>10</sup> Th. A. Mueller,<sup>10</sup> A. D. Santos,<sup>10</sup> P. Paganini,<sup>10</sup> B. Quilain,<sup>10</sup> R. Rogly,<sup>10</sup> T. Nakamura,<sup>11</sup> J. S. Jang,<sup>12</sup> L. N. Machado,<sup>13</sup> J. G. Learned,<sup>14</sup> K. Choi,<sup>15</sup> N. Iovine,<sup>15</sup> S. Cao,<sup>16</sup> L. H. V. Anthony,<sup>17</sup> D. Martin,<sup>17</sup> N. W. Prouse,<sup>17</sup> M. Scott,<sup>17</sup> Y. Uchida,<sup>17</sup> V. Berardi,<sup>18</sup> N. F. Calabria,<sup>18</sup> M. G. Catanesi,<sup>18</sup> E. Radicioni,<sup>18</sup> A. Langella,<sup>19</sup> G. De Rosa,<sup>19</sup> G. Collazuol,<sup>20</sup> F. Iacob,<sup>20</sup> M. Mattiazzi,<sup>20</sup> L. Ludovici,<sup>21</sup> M. Gonin,<sup>22</sup> G. Pronost,<sup>22</sup> C. Fujisawa,<sup>23</sup> Y. Maekawa,<sup>23</sup> Y. Nishimura,<sup>23</sup> R. Okazaki,<sup>23</sup> R. Akutsu,<sup>24</sup> M. Friend,<sup>24</sup> T. Hasegawa,<sup>24</sup> T. Ishida,<sup>24</sup> T. Kobayashi,<sup>24</sup> M. Jakkpu,<sup>24</sup> T. Matsubara,<sup>24</sup> T. Nakadaira,<sup>24</sup> K. Nakamura,<sup>24,48</sup> Y. Oyama,<sup>24</sup> K. Sakashita,<sup>24</sup> T. Sekiguchi,<sup>24</sup> T. Tsukamoto,<sup>24</sup> N. Bhuiyan,<sup>25</sup> G. T. Burton,<sup>25</sup> F. Di Lodovico,<sup>25</sup> J. Gao,<sup>25</sup> A. Goldsack,<sup>25</sup> T. Katori,<sup>25</sup> J. Migenda,<sup>25</sup> R. M. Ramsden,<sup>25</sup> Z. Xie,<sup>25</sup> S. Zsoldos,<sup>25,48</sup> A. T. Suzuki,<sup>26</sup> Y. Takagi,<sup>26</sup> Y. Takeuchi,<sup>26,48</sup> H. Zhong,<sup>26</sup> J. Feng,<sup>27</sup> L. Feng,<sup>27</sup> J. R. Hu,<sup>27</sup> Z. Hu,<sup>27</sup> M. Kawauae,<sup>27</sup> T. Kikawa,<sup>27</sup> M. Mori,<sup>27</sup> T. Nakaya,<sup>27,48</sup> R. A. Wendell,<sup>27,48</sup> K. Yasutome,<sup>27</sup> S. J. Jenkins,<sup>28</sup> N. McCauley,<sup>28</sup> P. Mehta,<sup>28</sup> A. Tarrant,<sup>28</sup> M. J. Wilking,<sup>29</sup> Y. Fukuda,<sup>30</sup> Y. Itow,<sup>31,32</sup> H. Menjo,<sup>31</sup> K. Ninomiya,<sup>31</sup> Y. Yoshioka,<sup>31</sup> J. Lagoda,<sup>33</sup> M. Mandal,<sup>33</sup> P. Mijakowski,<sup>33</sup> Y. S. Prabhu,<sup>33</sup> J. Zalipska,<sup>33</sup> M. Jia,<sup>34</sup> J. Jiang,<sup>34</sup> W. Shi,<sup>34</sup> C. Yanagisawa,<sup>34,\*</sup> M. Harada,<sup>35</sup> Y. Hino,<sup>35</sup> H. Ishino,<sup>35</sup> Y. Koshio,<sup>35,48</sup> F. Nakanishi,<sup>35</sup> S. Sakai,<sup>35</sup> T. Tada,<sup>35</sup> T. Tano,<sup>35</sup> T. Ishizuka,<sup>36</sup> G. Barr,<sup>37</sup> D. Barrow,<sup>37</sup> L. Cook,<sup>37,48</sup> S. Samani,<sup>37</sup> D. Wark,<sup>37,43</sup> A. Holin,<sup>38</sup> F. Nova,<sup>38</sup> S. Jung,<sup>39</sup> B. S. Yang,<sup>39</sup> J. Y. Yang,<sup>39</sup> J. Yoo,<sup>39</sup> J. E. P. Fannon,<sup>40</sup> L. Kneale,<sup>40</sup> M. Malek,<sup>40</sup> J. M. McElwee,<sup>40</sup> M. D. Thiesse,<sup>40</sup> L. F. Thompson,<sup>40</sup> S. T. Wilson,<sup>40</sup> H. Okazawa,<sup>41</sup> S. M. Lakshmi,<sup>42</sup> S. B. Kim,<sup>44</sup> E. Kwon,<sup>44</sup> J. W. Seo,<sup>44</sup> I. Yu,<sup>44</sup> A. K. Ichikawa,<sup>45</sup> K. D. Nakamura,<sup>45</sup> S. Tairafune,<sup>45</sup> K. Nishijima,<sup>46</sup> A. Eguchi,<sup>47</sup> K. Nakagiri,<sup>47</sup> Y. Nakajima,<sup>47,48</sup> S. Shima,<sup>47</sup> N. Taniuchi,<sup>47</sup> E. Watanabe,<sup>47</sup> M. Yokoyama,<sup>47,48</sup> P. de Perio,<sup>48</sup> S. Fujita,<sup>48</sup> C. Jesùs-Valls,<sup>48</sup> K. Martens,<sup>48</sup> K. M. Tsui,<sup>48</sup> M. R. Vagins,<sup>48,6</sup> J. Xia,<sup>48</sup> S. Izumiymaya,<sup>49</sup> M. Kuze,<sup>49</sup> R. Matsumoto,<sup>49</sup> M. Ishitsuka,<sup>50</sup> H. Ito,<sup>50</sup> Y. Ommura,<sup>50</sup> N. Shigeta,<sup>50</sup> M. Shinoki,<sup>50</sup> K. Yamauchi,<sup>50</sup> T. Yoshida,<sup>50</sup> R. Gaur,<sup>51</sup> V. Gousy-Leblanc,<sup>51,†</sup> M. Hartz,<sup>51</sup> A. Konaka,<sup>51</sup> X. Li,<sup>51</sup> S. Chen,<sup>52</sup> B. D. Xu,<sup>52</sup> B. Zhang,<sup>52</sup> M. Posiadala-Zezula,<sup>53</sup> S. B. Boyd,<sup>54</sup> R. Edwards,<sup>54</sup> D. Hadley,<sup>54</sup> M. Nicholson,<sup>54</sup> M. O'Flaherty,<sup>54</sup> B. Richards,<sup>54</sup> A. Ali,<sup>55,51</sup> B. Jamieson,<sup>55</sup> S. Amanai,<sup>56</sup> Ll. Martí,<sup>56</sup> A. Minamino,<sup>56</sup> and S. Suzuki<sup>56</sup>

(The Super-Kamiokande Collaboration)

<sup>1</sup>Kamioka Observatory, Institute for Cosmic Ray Research, University of Tokyo, Kamioka, Gifu 506-1205, Japan

<sup>2</sup>Research Center for Cosmic Neutrinos, Institute for Cosmic Ray Research, University of Tokyo, Kashiwa, Chiba 277-8582, Japan

<sup>3</sup>Department of Theoretical Physics, University Autònoma Madrid, 28049 Madrid, Spain

<sup>4</sup>Department of Physics, Boston University, Boston, MA 02215, USA

<sup>5</sup>Department of Physics, British Columbia Institute of Technology, Burnaby, BC, V5G 3H2, Canada

<sup>6</sup>Department of Physics and Astronomy, University of California, Irvine, Irvine, CA 92697-4575, USA

<sup>7</sup>Department of Physics, California State University, Dominguez Hills, Carson, CA 90747, USA

<sup>8</sup>Institute for Universe and Elementary Particles, Chonnam National University, Gwangju 61186, Korea

<sup>9</sup>Department of Physics, Duke University, Durham NC 27708, USA

<sup>10</sup>Ecole Polytechnique, IN2P3-CNRS, Laboratoire Leprince-Ringuet, F-91120 Palaiseau, France

<sup>11</sup>Department of Physics, Gifu University, Gifu, Gifu 501-1193, Japan

<sup>12</sup>GIST College, Gwangju Institute of Science and Technology, Gwangju 500-712, Korea

<sup>13</sup>School of Physics and Astronomy, University of Glasgow, Glasgow, Scotland, G12 8QQ, United Kingdom

<sup>14</sup>Department of Physics and Astronomy, University of Hawaii, Honolulu, HI 96822, USA

<sup>15</sup>Center for Underground Physics, Institute for Basic Science (IBS), Daejeon, 34126, Korea

<sup>16</sup>Institute For Interdisciplinary Research in Science and Education, ICISE, Quy Nhon, 55121, Vietnam

<sup>17</sup>Department of Physics, Imperial College London , London, SW7 2AZ, United Kingdom

<sup>18</sup>Dipartimento Interuniversitario di Fisica, INFN Sezione di Bari and Università e Politecnico di Bari, I-70125, Bari, Italy

<sup>19</sup>Dipartimento di Fisica, INFN Sezione di Napoli and Università di Napoli, I-80126, Napoli, Italy

<sup>20</sup>Dipartimento di Fisica, INFN Sezione di Padova and Università di Padova, I-35131, Padova, Italy

<sup>21</sup>INFN Sezione di Roma and Università di Roma "La Sapienza", I-00185, Roma, Italy

<sup>57</sup> <sup>22</sup> ILANCE, CNRS - University of Tokyo International Research Laboratory, Kashiwa, Chiba 277-8582, Japan

<sup>58</sup> <sup>23</sup> Department of Physics, Keio University, Yokohama, Kanagawa, 223-8522, Japan

<sup>59</sup> <sup>24</sup> High Energy Accelerator Research Organization (KEK), Tsukuba, Ibaraki 305-0801, Japan

<sup>60</sup> <sup>25</sup> Department of Physics, King's College London, London, WC2R 2LS, UK

<sup>61</sup> <sup>26</sup> Department of Physics, Kobe University, Kobe, Hyogo 657-8501, Japan

<sup>62</sup> <sup>27</sup> Department of Physics, Kyoto University, Kyoto, Kyoto 606-8502, Japan

<sup>63</sup> <sup>28</sup> Department of Physics, University of Liverpool, Liverpool, L69 7ZE, United Kingdom

<sup>64</sup> <sup>29</sup> School of Physics and Astronomy, University of Minnesota, Minneapolis, MN 55455, USA

<sup>65</sup> <sup>30</sup> Department of Physics, Miyagi University of Education, Sendai, Miyagi 980-0845, Japan

<sup>66</sup> <sup>31</sup> Institute for Space-Earth Environmental Research, Nagoya University, Nagoya, Aichi 464-8602, Japan

<sup>67</sup> <sup>32</sup> Kobayashi-Maskawa Institute for the Origin of Particles and the Universe, Nagoya University, Nagoya, Aichi 464-8602, Japan

<sup>68</sup> <sup>33</sup> National Centre For Nuclear Research, 02-093 Warsaw, Poland

<sup>69</sup> <sup>34</sup> Department of Physics and Astronomy, State University of New York at Stony Brook, NY 11794-3800, USA

<sup>70</sup> <sup>35</sup> Department of Physics, Okayama University, Okayama, Okayama 700-8530, Japan

<sup>71</sup> <sup>36</sup> Media Communication Center, Osaka Electro-Communication University, Neyagawa, Osaka, 572-8530, Japan

<sup>72</sup> <sup>37</sup> Department of Physics, Oxford University, Oxford, OX1 3PU, United Kingdom

<sup>73</sup> <sup>38</sup> Rutherford Appleton Laboratory, Harwell, Oxford, OX11 0QX, UK

<sup>74</sup> <sup>39</sup> Department of Physics, Seoul National University, Seoul 151-742, Korea

<sup>75</sup> <sup>40</sup> Department of Physics and Astronomy, University of Sheffield, S3 7RH, Sheffield, United Kingdom

<sup>76</sup> <sup>41</sup> Department of Informatics in Social Welfare, Shizuoka University of Welfare, Yaizu, Shizuoka, 425-8611, Japan

<sup>77</sup> <sup>42</sup> August Cichkowski Institute of Physics, University of Silesia in Katowice, 75 Putku Piechoty 1, 41-500 Chorzów, Poland

<sup>78</sup> <sup>43</sup> STFC, Rutherford Appleton Laboratory, Harwell Oxford, and

<sup>79</sup> Daresbury Laboratory, Warrington, OX11 0QX, United Kingdom

<sup>80</sup> <sup>44</sup> Department of Physics, Sungkyunkwan University, Suwon 440-746, Korea

<sup>81</sup> <sup>45</sup> Department of Physics, Faculty of Science, Tohoku University, Sendai, Miyagi, 980-8578, Japan

<sup>82</sup> <sup>46</sup> Department of Physics, Tokai University, Hiratsuka, Kanagawa 259-1292, Japan

<sup>83</sup> <sup>47</sup> Department of Physics, University of Tokyo, Bunkyo, Tokyo 113-0033, Japan

<sup>84</sup> <sup>48</sup> Kavli Institute for the Physics and Mathematics of the Universe (WPI), The University of

<sup>85</sup> Tokyo Institutes for Advanced Study, University of Tokyo, Kashiwa, Chiba 277-8583, Japan

<sup>86</sup> <sup>49</sup> Department of Physics, Tokyo Institute of Technology, Meguro, Tokyo 152-8551, Japan

<sup>87</sup> <sup>50</sup> Department of Physics, Faculty of Science and Technology, Tokyo University of Science, Noda, Chiba 278-8510, Japan

<sup>88</sup> <sup>51</sup> TRIUMF, 4004 Wesbrook Mall, Vancouver, BC, V6T2A3, Canada

<sup>89</sup> <sup>52</sup> Department of Engineering Physics, Tsinghua University, Beijing, 100084, China

<sup>90</sup> <sup>53</sup> Faculty of Physics, University of Warsaw, Warsaw, 02-093, Poland

<sup>91</sup> <sup>54</sup> Department of Physics, University of Warwick, Coventry, CV4 7AL, UK

<sup>92</sup> <sup>55</sup> Department of Physics, University of Winnipeg, MB R3J 3L8, Canada

<sup>93</sup> <sup>56</sup> Department of Physics, Yokohama National University, Yokohama, Kanagawa, 240-8501, Japan

(Dated: December 26, 2024)

We present measurements of neutron production from atmospheric neutrino interactions in water, analyzed as a function of the electron-equivalent visible energy, ranging from 30 MeV to 10 GeV. These results are based on 4,270 days of data collected by Super-Kamiokande, including 564 days with 0.011 wt% gadolinium added to enhance neutron detection. The measurements are compared to predictions from neutrino event generators combined with models of secondary interactions including hadron transport and nuclear de-excitation. Notably, the predictions varied significantly depending on the secondary interaction model used. The Liège model (INCL++) coupled with Geant4 Precompound model showed better agreement with our observations across the entire energy range, compared to the widely used Geant4 Bertini cascade model and its variants. We further discuss the model-specific features contributing to these variations in predictions.

## I. INTRODUCTION

A significant fraction of neutrino experiments rely on nuclear targets, yet considerable uncertainty remains on how quantum correlations among nucleons affect interaction cross sections and outgoing particle kinematics.

Modeling these so-called “nuclear effects” is especially critical for GeV-scale neutrino experiments, which aim precise measurement of neutrino oscillation, including CP violation and neutrino mass ordering. Outgoing hadrons are valuable probes of these nuclear effects, and recent advances in neutrino detectors have enabled precise measurements of hadron multiplicities and kinematics from neutrino interactions. Notably, measurements of proton production in neutrino interactions with liquid Argon have revealed several discrepancies between observed and predicted distributions of kinematic observables [1].

\* also at BMCC/CUNY, Science Department, New York, New York, 1007, USA.

† also at University of Victoria, Department of Physics and Astronomy, PO Box 1700 STN CSC, Victoria, BC V8W 2Y2, Canada.

122 Neutrons hold a unique status in neutrino experiments,  
 123 as they do not leave ionization tracks, making their iden-  
 124 tification inherently challenging. In tracking detectors,  
 125 neutrons are primarily identified through displaced pro-  
 126 ton tracks, which limits detection efficiency due to the  
 127 subdominant ( $n, p$ ) reaction cross section [2]. This poses  
 128 a particular challenge for reconstructing neutrino interac-  
 129 tions in the few-GeV energy range, where neutrons often  
 130 carry a significant fraction of the neutrino's energy. Acc-  
 131 curate estimation of this "missing energy" is critical, as  
 132 errors can introduce biases in key measurements, such as  
 133 the determination of the Dirac CP phase [3].

134 Neutrons can also be detected via the radiative neutron  
 135 capture ( $n, \gamma$ ) reaction, which has no practical energy  
 136 threshold. Neutrons with kinetic energies of a few MeV  
 137 or lower are likely to thermalize, undergoing ( $n, \gamma$ ) reac-  
 138 tions with well-defined timescales and energy signatures  
 139 that enable clean signal selection. This characteristic his-  
 140 torically made neutrons effective tags for antineutrino  
 141 charged-current (CC) interactions (e.g.,  $\bar{\nu}_\mu p \rightarrow \mu^+ n$ )  
 142 compared to neutrino interactions (e.g.,  $\nu_\mu n \rightarrow \mu^- p$ ).  
 143 Neutron tagging remains relevant today, for instance, in  
 144 atmospheric neutrino oscillation analyses, where it en-  
 145 hances sensitivity to both neutrino mass ordering and CP<sup>180</sup>  
 146 violation, by preventing the cancellation of opposite-sign<sup>181</sup>  
 147 effects in neutrino and antineutrino oscillation probabili-<sup>182</sup>  
 148 ties [4]. Additionally, neutron tagging helps suppress at-<sup>183</sup>  
 149 mospheric neutrino backgrounds for rare events, such as<sup>184</sup>  
 150 proton decay (e.g.,  $p \rightarrow e^+ \pi^0$  [5]), which in many cases is<sup>185</sup>  
 151 not expected to produce neutrons, or inverse beta decay<sup>186</sup>  
 152 ( $\bar{\nu}_e p \rightarrow e^+ n$ ) induced by supernova  $\bar{\nu}_e$ , which typically<sup>187</sup>  
 153 produces only one neutron. Accurately predicting the<sup>188</sup>  
 154 number of detectable neutrons from neutrino interactions<sup>189</sup>  
 155 is crucial for these analyses and requires well-constrained<sup>190</sup>  
 156 uncertainties in interaction models.<sup>191</sup>

157 Several studies have measured neutron production<sup>192</sup>  
 158 from atmospheric or artificial neutrino interactions using<sup>193</sup>  
 159 water (T2K [6]), heavy water (SNO [7]), and hydrocar-<sup>194</sup>  
 160 bon (MINERvA [8, 9]) as target materials. These studies<sup>195</sup>  
 161 consistently reported deficits in observed neutron signals<sup>196</sup>  
 162 compared to predictions from neutrino event generators,<sup>197</sup>  
 163 with the discrepancies often attributed to limitations in<sup>198</sup>  
 164 modeling the transport of secondary hadrons within the<sup>199</sup>  
 165 detector volume.<sup>200</sup>

166 The typical modeling approach used in these stud-<sup>201</sup>  
 167 ies is illustrated in Figure 1. Neutrino event gener-<sup>202</sup>  
 168 ators simulate outgoing hadrons from the initial neu-<sup>203</sup>  
 169 trino interaction, whether at the nucleon or quark level,<sup>204</sup>  
 170 and subsequently account for intranuclear hadron trans-<sup>205</sup>  
 171 port (commonly referred to as final-state interactions,<sup>206</sup>  
 172 or FSI), followed by nuclear de-excitation. Models for<sup>207</sup>  
 173 these latter processes are often used to describe inelastic<sup>208</sup>  
 174 hadron-nucleus collisions, which are typically simulated<sup>209</sup>  
 175 using particle transport codes such as Geant4. For clar-<sup>210</sup>  
 176 ity, we refer to the downstream hadron-induced interac-<sup>211</sup>  
 177 tions handled by particle transport codes as "secondary"<sup>212</sup>  
 178 hadron-nucleus interactions, distinguishing them from<sup>213</sup>  
 179 the "primary" neutrino-nucleus interaction.<sup>214</sup>

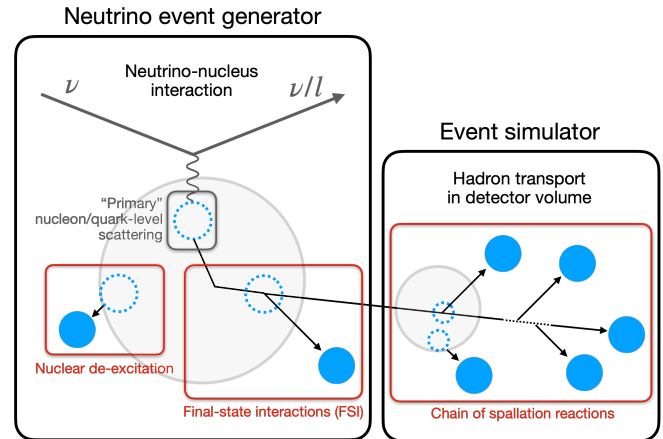


FIG. 1. Schematic of sources of nucleon production in a typical neutrino event simulation setup. Dashed blue circles represent nucleon holes, black arrows represent nucleon trajectories, and solid blue circles represent detectable nucleons ejected from nuclei.

Accurate prediction of the observable neutron multiplicity requires careful consideration of secondary neutron production. For hadron transport in the  $O(0.1-1)$  GeV energy range, semi-classical Intranuclear Cascade (INC) models [10] are commonly employed. These models approximate the process as a series of binary collisions between a hadron projectile and a quasi-free nucleon within the target nucleus. Subsequent nuclear de-excitation, modeled as a statistical process that releases neutrons with kinetic energies of a few MeV, also contribute significantly to neutron production at lower energies. Notably, variations in how these models account for nuclear effects often lead to significant discrepancies in predictions [11].

In this paper, we present a measurement of neutron production following atmospheric neutrino interactions in water. Using data from events fully contained within the Super-Kamiokande detector from 2008 to 2022, we evaluated the average multiplicity of ( $n, \gamma$ ) reactions (or "neutron captures") as a function of electron-equivalent visible energy, a calorimetric proxy for neutrino momentum transfer. These observations were compared with predictions generated using various models relevant to secondary neutron production.

This paper is structured as follows. Section II provides a brief overview of the SK detector. The selection process for atmospheric neutrino events and neutron signals, along with the estimation of selection performance, are detailed in Sections III and IV. Section V outlines the methodology for determining the average ( $n, \gamma$ ) multiplicity per visible energy bin and the associated systematic uncertainties. Section VI introduces the interaction models used for generating predictions. Finally, Sections VII and VIII present a comparison of observations with predictions and discuss the implications of the results.

TABLE I. SK operational phases and neutron-related characteristics. SK-IV, V, VI data were used in this analysis.

Phase	Dates	Livetime [days]	Gd concentration <sup>a</sup> [wt%]	H( $n, \gamma$ ) [%]	Expected ( $n, \gamma$ ) ratio <sup>b</sup> [%]	( $n, \gamma$ ) time constant <sup>c</sup> [ $\mu\text{s}$ ]
SK-I-III	1996-2008	2805.9	-	>99.9	-	No data
SK-IV	2008-2018	3244.4	-	>99.9	-	204.8 $\pm$ 9.8
SK-V	2019-2020	461.0	-	>99.9	-	199.8 $\pm$ 10.2
SK-VI	2020-2022	564.4 <sup>d</sup>	0.0110 $\pm$ 0.0001 [13]	56.1 $\pm$ 1.5	43.9 $\mp$ 1.5	116.2 $\pm$ 2.3
SK-VII-VIII	2022-present	-	0.0332 $\pm$ 0.0002 [14]	29.7 $\pm$ 0.7	70.3 $\mp$ 0.7	61.8 $\pm$ 0.1 [14]

<sup>a</sup> Based on the amount of dissolved Gd.

<sup>b</sup> Based on the evaluated thermal ( $n, \gamma$ ) reaction cross sections and uncertainties of ENDF/B-VII.1 [12].

<sup>c</sup> Weighted mean of all Am/Be neutron source measurements, explained in Section IV B.

<sup>d</sup> Excludes earlier runs which showed signs of non-uniform Gd concentration, i.e., varying time constant by position.

## II. THE SUPER-KAMIOKANDE DETECTOR

Super-Kamiokande (SK) [15] is an underground water Cherenkov detector located in Gifu, Japan. It consists of two optically separated, concentric cylindrical volumes: the inner detector (ID) containing 32.5 ktons of water and equipped with 11,129 inward-facing photomultiplier tubes (PMTs) and the outer detector serving as a cosmic-ray veto. The detector registers a PMT signal with over 0.25 photoelectron-equivalent charge as a “hit”. If the number of ID or OD PMT hits within a 200-ns sliding time window ( $N_{200\text{-ns}}$ ) exceeds a given threshold, an event trigger is issued. The details of the detector can be found in [15, 16].

Charged particles, namely electrons and muons produced by charged-current neutrino interactions, are identified through Cherenkov radiation. The radiation is projected onto the PMTs as a characteristic ring pattern with an opening angle of approximately 42 degrees from the initial vertex. This ring pattern serves as the basis for particle reconstruction. Neutrons are indirectly identified via Compton-scattered electrons resulting from ( $n, \gamma$ ) reactions. In pure water, most occur on  $^1\text{H}$ , emitting a single 2.2 MeV gamma-ray. With the recent addition of gadolinium (Gd), the majority of neutrons are expected to be captured by Gd isotopes, resulting in a total gamma-radiated energy of around 8 MeV.

The  $O(1)$  MeV signal identification performance is significantly influenced by variations in detector characteristics. Parameters such as individual PMT gain, timing properties, quantum efficiency, and optical absorption and scattering in water are continuously monitored using cosmic-ray muons and light sources [16]. Additionally, the uncertainty in Cherenkov ring energy reconstruction (described in Section III B) is evaluated over a wide energy range using naturally occurring particles, including cosmic-ray muons, Michel electrons, and neutral pions produced in neutral-current (NC) atmospheric neutrino interactions in water. Figure 2 illustrates the agreement between data and simulation in energy reconstruction for the Gd-loaded SK-VI phase, which is mostly within 2% across the  $O(10\text{-}10^4)$  MeV range and consistent with the pure water phase results reported in [4].

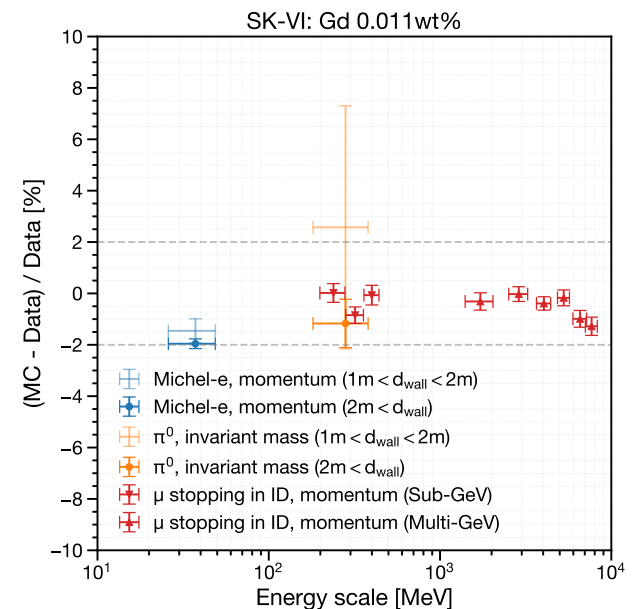


FIG. 2. Comparison of energy reconstruction performance between Monte Carlo (MC) simulation and observed data for naturally occurring particles in the Gd-loaded SK-VI phase. The variable  $d_{\text{wall}}$  represents the distance (in meters) from the reconstructed vertex to the nearest ID photodetector wall. The fiducial volume for this study is defined as  $d_{\text{wall}} > 1$  m.

The detector has operated through eight different phases. Neutron detection began with the fourth phase SK-IV, following the electronics upgrade [17] that allowed extended event recording up to 535  $\mu\text{s}$  after certain ID triggers. This has enabled analysis of delayed neutron captures that occur with a time scale of  $O(10\text{-}100)$   $\mu\text{s}$  following an atmospheric neutrino interaction. Between SK-IV and SK-V, in 2018, the detector underwent refurbishment, during which malfunctioning PMTs were replaced. The later phases, SK-VI, SK-VII, and SK-VIII involved the dissolution of  $\text{Gd}_2(\text{SO}_4)_3$  into the water volume to enhance neutron detection efficiency [13, 14]. Table I summarizes the relevant operational conditions.

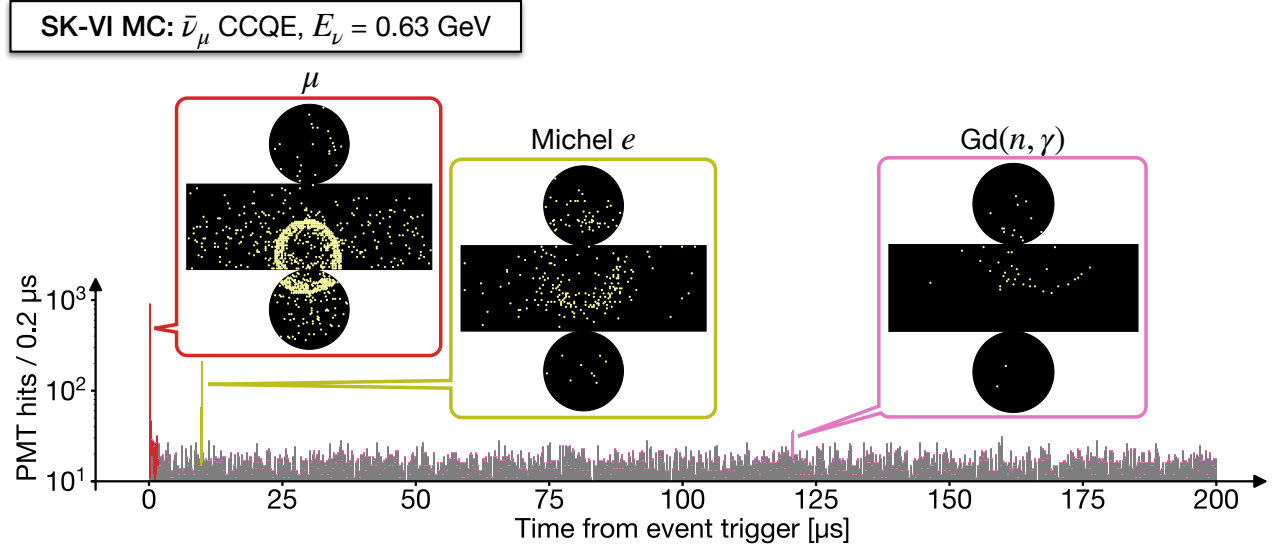


FIG. 3. A PMT hit time distribution for a typical  $\bar{\nu}_\mu$  charged-current (CC) quasi-elastic (QE) interaction with a muon and a neutron as final states. The zero is set at the event trigger. The event displays feature the “prompt” muon signal (red) and the two types of “delayed” coincident signals — Michel electrons from muon decay (olive) and neutron captures on Gd (pink). The gray bars represent randomly recorded background PMT hits. This event was simulated in the SK-VI configuration.

### 270 III. ATMOSPHERIC NEUTRINO EVENTS

#### 271 A. Data reduction

272 We followed a typical selection process for atmospheric  
273 neutrino interactions that are fully contained within the  
274 ID, similar to previous studies conducted at SK [4]. All  
275 events were required to pass the ID trigger with the  
276 threshold  $N_{200\text{-ns}} \geq 58$  PMT hits—roughly correspond-  
277 ing to a 10 MeV electron—followed by the extended 535  
278  $\mu$ s event window for neutron detection.

279 Selected events were reconstructed as described in Sec-  
280 tion III B. To further reject low-energy backgrounds, we  
281 required that the reconstructed vertex be more than 1 m  
282 away from the ID tank wall (defining the fiducial volume  
283 with 23.2 kton of water) and that the visible energy be  
284 larger than 30 MeV. The remaining background contam-  
285 ination, mainly due to corner-clipping cosmic-ray muons  
286 and PMT discharges, was estimated to be below 0.2%,  
287 based on visual inspection [5]. Additionally, events with  
288  $N_{200\text{-ns}} \geq 15$  PMT hits in the OD within 535  $\mu$ s from the  
289 event trigger were considered indicative of delayed cap-  
290 tures of neutrons escaping the tank and were rejected.

#### 291 B. Reconstruction of prompt Cherenkov rings

292 Figure 3 shows a PMT hit time distribution of a typi-  
293 cal  $\bar{\nu}_\mu$  charged-current (CC) quasi-elastic (QE) event fol-  
294 lowed by a Michel electron and a Gd( $n, \gamma$ ) reaction, along  
295 with the corresponding event displays. For the “prompt”  
296 radiation due to charged particles (namely, electrons and

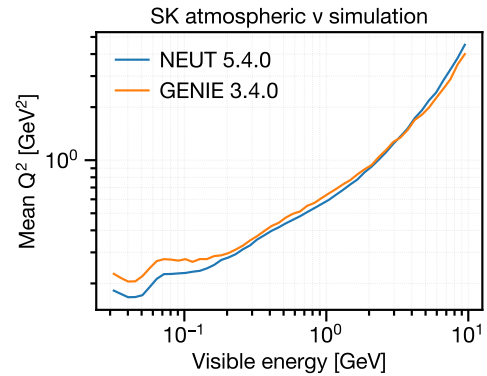


FIG. 4. Average squared momentum transfer ( $Q^2$ ) per visible energy bin for simulated atmospheric neutrino events at SK, compared between two different neutrino event generators. NEUT 5.4.0 (blue) uses the baseline setup described in Section III C, while GENIE 3.4.0 [18–20] uses the “hN” setup as described in Section VI. The vertical error bars represent standard errors associated with the mean  $Q^2$  per each bin.

297 muons) produced via the primary neutrino interaction,  
298 we followed the typical Cherenkov ring reconstruction  
299 process [21] as applied in previous SK analyses [4, 5].

300 The visible energy of an event is defined as the sum of  
the reconstructed kinetic energies of all Cherenkov rings,  
assuming each ring originates from an electron. This  
calorimetric measure serves as a reliable proxy for neu-  
trino momentum transfer, as demonstrated by the pos-  
itive correlation shown in Figure 4.

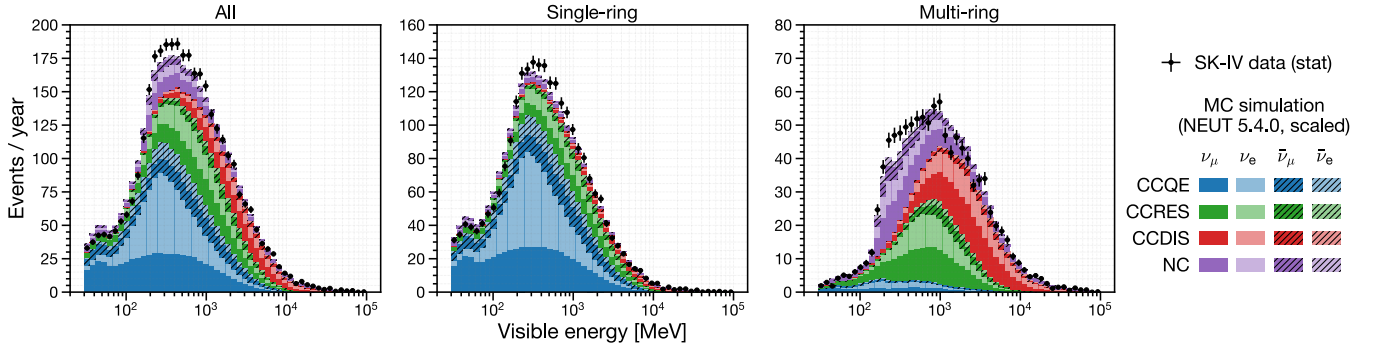


FIG. 5. Visible energy distributions for observed and simulated atmospheric neutrino interactions in water, fully contained within the fiducial volume: all events (left), events with one reconstructed Cherenkov ring (middle), and events with two or more rings (right). CCQE events dominate the single-ring sample, while RES and DIS events dominate the multi-ring sample. The simulation setup is detailed in Section III C. Simulated distributions are scaled to match the SK-IV data to account for neutrino flux uncertainties.

306

### C. Baseline simulation setup

The simulation of atmospheric neutrino events involves<sup>346</sup>  
<sup>347</sup> a convolution of the atmospheric neutrino flux, neutrino<sup>347</sup>  
<sup>348</sup> event generator, and detector simulation.<sup>348</sup>

To determine the incoming neutrino kinematics and<sup>349</sup>  
<sup>350</sup> event rate, we used atmospheric flux calculations for  $\nu_e$ ,<sup>350</sup>  
<sup>351</sup>  $\nu_\mu$ ,  $\bar{\nu}_e$ , and  $\bar{\nu}_\mu$  at the detector site, assuming no oscillations,<sup>351</sup>  
<sup>352</sup> as provided by Honda et al. [22] for neutrino energies<sup>352</sup>  
<sup>353</sup> ranging from 100 MeV to 10 TeV. Interactions of  $\nu_\tau$ <sup>353</sup>  
<sup>354</sup> and  $\bar{\nu}_\tau$  were not simulated.<sup>354</sup>

Neutrino interactions in water were modeled using neutrino<sup>355</sup>  
<sup>356</sup> event generators [23], which compute the cross sections<sup>356</sup>  
<sup>357</sup> for each interaction channel and sample outgoing<sup>357</sup>  
<sup>358</sup> particle kinematics. NEUT 5.4.0 [24] was used as the<sup>358</sup>  
<sup>359</sup> baseline event generator. It covers major interaction<sup>359</sup>  
<sup>360</sup> channels, including QE scattering with single (1p1h) or<sup>360</sup>  
<sup>361</sup> double (2p2h) nucleon knockout, single pion production<sup>361</sup>  
<sup>362</sup> due to  $\Delta$  resonance (RES), and multiple pion production<sup>362</sup>  
<sup>363</sup> via deep inelastic scattering (DIS). The models used<sup>363</sup>  
<sup>364</sup> are consistent with the latest SK atmospheric neutrino<sup>364</sup>  
<sup>365</sup> oscillation analysis [4].<sup>365</sup>

The transport of hadronic final states within the target<sup>366</sup>  
<sup>367</sup> nucleus (FSI) was modeled separately from the primary<sup>367</sup>  
<sup>368</sup> neutrino interaction. The transport of low-momentum<sup>368</sup>  
<sup>369</sup> ( $< 500$  MeV/c) pions was based on Salcedo et al. [25],<sup>369</sup>  
<sup>370</sup> with parameters tuned to fit external pion-nucleus scattering<sup>370</sup>  
<sup>371</sup> data [26]. For higher energy nucleons and pions,<sup>371</sup>  
<sup>372</sup> FSIs were modeled using the INC approach, which includes<sup>372</sup>  
<sup>373</sup> elastic scattering and single/double pion production.<sup>373</sup>  
<sup>374</sup> The cross sections for reactions with free target<sup>374</sup>  
<sup>375</sup> nucleons were sourced from Bertini [27] for nucleon projectiles<sup>375</sup>  
<sup>376</sup> and from external pion scattering data for high-momentum<sup>376</sup>  
<sup>377</sup> pion projectiles [28]. The de-excitation of an oxygen target<sup>377</sup>  
<sup>378</sup> was modeled using tabulated occupation probabilities for<sup>378</sup>  
<sup>379</sup> nucleon energy states [29] and branch ratios for knockout of<sup>379</sup>  
<sup>380</sup> each state [30].<sup>380</sup>

The subsequent particle transport in water and detector<sup>381</sup>  
<sup>382</sup> responses were simulated using Geant3.21 [31].<sup>382</sup>

344

Hadron propagation above 10 GeV was simulated using FLUKA [32], while GCALOR, based on the Bertini cascade model [33] as implemented in NMTC [34], was used for energies below 10 GeV. For low-energy neutrons with kinetic energy below 20 MeV, GCALOR calls MICAP [35], using ENDF/B-V [36] cross sections. The transport of low-momentum pions was separately modeled using the NEUT pion FSI routine to ensure consistency between NEUT and Geant3.

For the transport of low-energy neutrons in the Gd-loaded SK-VI phase, we imported reaction cross sections from the Geant4.10.03.p01 [37–39] NeutronHP database [40] based on ENDF/B-VII.1 [12], replacing MICAP for neutron energies below 20 MeV. Additionally, we modeled the gamma-cascade resulting from neutron captures on <sup>155/157</sup>Gd using the ANNRI-Gd model [41, 42].

The characteristics of individual PMTs and the optical parameters in water were adjusted to align with calibration data obtained from light sources and through-going cosmic-ray muons. To accurately account for detector noise, randomly recorded PMT hits were included as background, represented as gray bars in Figure 3.

500 years of atmospheric neutrino events were simulated for each SK phase and processed as described in Sections III B and III A. The events in the final sample were weighted based on the standard three-flavor oscillation probability in matter [43], using the oscillation parameters fitted with reactor constraints in the previous SK analysis [44] and the PREM model [45] for Earth's matter density. Corrections for atmospheric neutrino flux accounting for solar activity were also applied.

Figure 5 shows the visible energy distributions of the simulated event sample, demonstrating reasonable agreement with the observations. Single-ring events exhibit a higher fraction of QE interactions and a smaller fraction of DIS compared to multi-ring events. For the same visible energy, multi-ring events are expected to produce more secondary neutrons than single-ring events, due to a higher fraction of DIS interactions with larger  $W$ .

## IV. NEUTRON SIGNAL SELECTION

384 Neutrons produced by atmospheric neutrino interactions in the SK ID are primarily captured by  $^1\text{H}$  or  
 385  $^{155}/^{157}\text{Gd}$  isotopes within approximately  $O(100)$   $\mu\text{s}$ , with  
 386 expected capture ratios summarized in Table I. Electrons that are scattered by the  $O(1)$  MeV gamma-rays generate Cherenkov photons that form faint rings on the ID tank wall (hereafter referred to as “neutron signal”), as shown in Figure 3.

392 Fast neutrons, along with the subsequent gamma-rays and scattered electrons, typically travel only a few tens of centimeters in water. Thus, signal photons can be approximated as originating from a single vertex. While reconstructing this vertex is challenging due to the limited number of PMT hits, *assuming* it to be near another known vertex, such as the reconstructed neutrino interaction vertex, helps identify signals from random PMT coincidences caused by dark current. Remaining Michel electrons from muon decays can be effectively suppressed through cuts based on signal timing and energy.

### A. Signal selection algorithm

404 The signal selection algorithm is based on Ref. [46], and consists of two stages.

406 In the first candidate search stage, we initially subtract the expected photon time-of-flight (ToF) from the individual PMT hit times for a given *assumed* signal vertex, which was provided by the reconstructed neutrino event vertex. Then, we slide a time window of 14 ns width on the ToF-corrected PMT hit times to trigger on the number of included PMT hits. The threshold was 5 for pure water phases SK-IV and V, and 7 for the Gd-loaded phase SK-VI. The search span for each event was [18, 534]  $\mu\text{s}$  from the event trigger for SK-IV and V, and [3, 534]  $\mu\text{s}$  for SK-VI with a shorter neutron capture time. For overlapping candidates within 50 ns, only the candidate with the largest number of PMT hits is selected.

419 In the second candidate classification stage, we extract features of each candidate and use a neural network to classify each candidate into signal and noise based on input features. These features characterize the signal energy, the background hit level, timing spread assuming the vertex, correlation between the input vertex and the hit PMT positions, correlation to the known properties of PMT noise, and angular correlation among hit PMTs relative to the Cherenkov cone opening angle.

428 The major changes from the original algorithm [46] include a simplified algorithm, a reduced set of features, and a heuristically tuned neural network architecture. These modifications aim to reduce performance bias between the data and the simulation that is used to train the neural networks.

434 Here, we provide the definition and unit of each feature used for the classification of signal candidates, along with their expected distributions as shown in Figure 6:

- **NHits**

The number of selected PMT hits within the 14-ns sliding time window.

- **NResHits**

The number of PMT hits within [-100,+100] ns from the center of the 14-ns sliding time window, subtracted from NHits.

- **TRMS** [ns]

The root mean square (RMS) of the ToF-corrected time distribution of the selected PMT hits.

- **FitGoodness**

The normalized likelihood of the ToF-corrected time distribution of the selected PMT hits, given the *assumed* signal vertex and the Gaussian PMT timing resolution of 5 ns.

- **DWall** [cm]

The distance from the *assumed* signal vertex to the nearest tank wall.

- **DWallMeanDir** [cm]

The shorter of the radial and vertical distances from the *assumed* signal vertex to the tank wall, weighted by the mean of the unit vectors connecting the vertex to each hit PMT.

- **BurstRatio**

The ratio of the selected PMTs with a preceding hit within 10  $\mu\text{s}$ , which are likely caused by scintillation within the irradiated PMT glass.

- **DarkLikelihood**

The normalized log likelihood ratio based on measured individual PMT dark rates, given by:

$$\text{DarkLikelihood} = \sigma \left( \log \prod_{i=1}^{\text{NHits}} \frac{r_i}{\langle r \rangle} \right) \quad (1)$$

where  $\sigma$  represents the sigmoid function,  $r_i$  is the dark rate of the  $i^{\text{th}}$  PMT, and  $\langle r \rangle$  is the average dark rate of all ID PMTs.

- **OpeningAngleStdev** [deg]

The standard deviation of the opening angles of cones formed by every possible combination of three hit PMTs and the *assumed* signal vertex.

- **Beta(k)**,  $k \in \{1, 2, 3, 4, 5\}$

$$\text{Beta}(k) = \frac{2}{\text{NHits}(\text{NHits} - 1)} \sum_{i \neq j} P_k(\cos \theta_{ij}) \quad (2)$$

where  $P_k$  is the  $k^{\text{th}}$  Legendre polynomial and  $\theta_{ij}$  is the opening angle between the assumed signal vertex and the  $i^{\text{th}}$  and  $j^{\text{th}}$  hit PMTs.

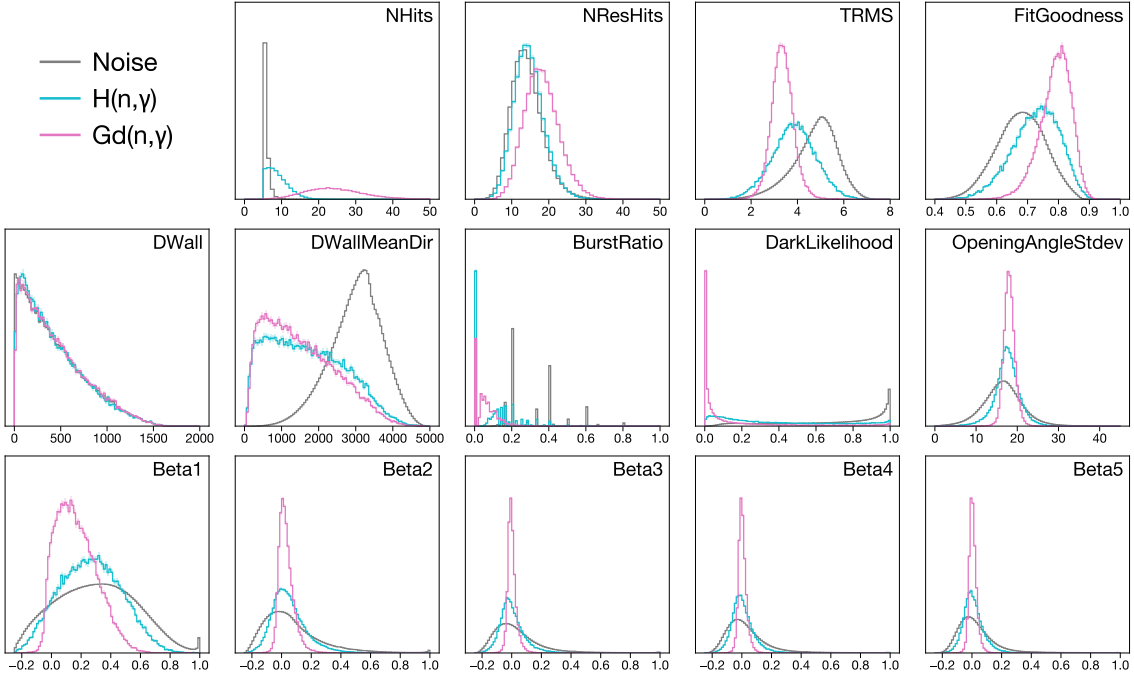


FIG. 6. The features (area-normalized) of neutron signals and noise from the thermal neutron MC simulation used for training the neural network for SK-VI phase.

For training the neural network, we utilized the features and labels of first-stage candidates from a particle-gun simulation of thermal neutrons, with vertices randomized within the ID. Each first-stage candidate, as shown in Figs. 6 and 7, was labeled as signal if it was triggered within 50 ns of the simulated  $(n, \gamma)$  reaction, and otherwise as background. Of the training dataset, 80% was used for updating the neural network weights, while the remaining 20% was reserved for validation.

We implemented a feed-forward fully connected neural network using Keras 2.6.0 [47]. The network consisted of an input layer with 14 features, followed by three dense layers, each comprising 128 ReLU-activated nodes with a 50% dropout rate, and a single sigmoid output node. Weights and biases were initialized following He et al. [48] and optimized by minimizing the binary cross-entropy loss iteratively on minibatches of size 2,048 using the Adam optimizer [49]. The initial learning rate was set to 0.0001. Training was stopped when signal efficiency on the validation set showed no improvement for 5 consecutive epochs. A neural network was trained for each SK phase: SK-IV, SK-V, and SK-VI.

Candidates with a neural network output greater than 0.7 were classified as signals, while those with a large number of PMT hits ( $N_{\text{Hits}} > 50$ ) and occurring earlier than the typical neutron capture timescale ( $< 20 \mu\text{s}$ ) were identified as Michel electrons and excluded. The effectiveness of this Michel electron rejection is illustrated in Figure 7. When applied to cosmic-ray muons decaying within the ID, the selection achieved an efficiency of  $98.4 \pm 1.3\%$  and a purity of  $98.7 \pm 0.5\%$ .

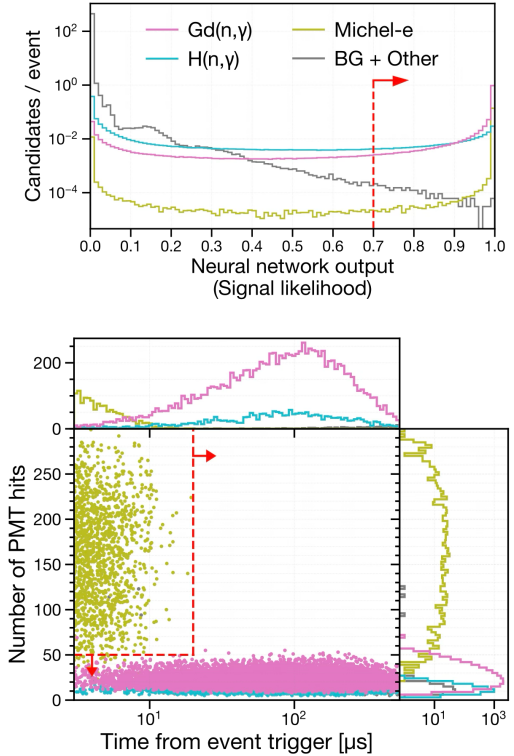


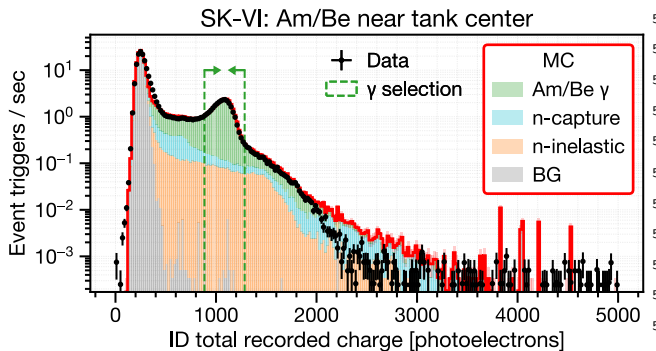
FIG. 7. The neural network response to neutron signals and backgrounds in the SK-VI atmospheric neutrino simulation (top), and the time versus energy distribution of signal candidates passing the neural network selection (bottom). Red arrows indicate the corresponding cut points.

## 511 B. Signal selection performance on calibration data

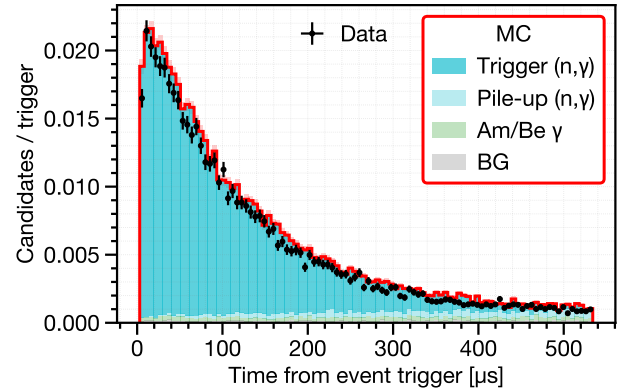
512 An Am/Be neutron source with a measured total intensity  
 513 of  $236.8 \pm 5.0$  neutrons/s [50] was used to obtain cal-  
 514 ibration data for estimating the signal detection perfor-  
 515 mance. The first-excited state of the alpha-absorbed  ${}^9\text{Be}$ ,  
 516 with a roughly 60% branching ratio, emits a fast neutron  
 517 and a 4.44 MeV gamma-ray simultaneously. This source  
 518 was encapsulated with Bismuth Germanate ( $\text{Bi}_4\text{Ge}_3\text{O}_{12}$ ,  
 519 BGO) crystals so that the 4.44 MeV gamma-rays can  
 520 induce scintillation. The setup was deployed in various  
 521 positions within the ID, and events were recorded for 30  
 522 minutes to 1 hour. Events with a trigger charge yield  
 523 corresponding to the 4.44 MeV gamma-ray scintillation  
 524 were regarded as the single neutron control sample.

525 The observed light yield distribution was compared  
 526 with dedicated simulation, as shown in Figure 8. The  
 527 simulation accounts for continuous source activity and  
 528 pile-up, by reorganizing the simulated detector response  
 529 to Am/Be neutron emission on a single global time axis,  
 530 based on the measured total neutron intensity and the es-  
 531 timated branching ratios to each excited state of alpha-  
 532 absorbed  ${}^9\text{Be}$ . As shown in Figure 8, this simulation  
 533 accurately models event triggers due to ambient neutron  
 534 captures and neutron inelastic interactions within scin-  
 535 tillator crystal. The contamination of such unwanted event  
 536 triggers in the 4.44 MeV gamma-ray event selection was  
 537 estimated to be at a few percent level.

538 Within the selected events in the single neutron con-  
 539 trol sample, signal candidates were obtained following the  
 540 algorithm described in Section IV A, with the *assumed*  
 541 signal vertex set at the source position.



561 FIG. 8. Distribution of recorded charge within the time  
 562 window  $[-0.5, 1.0]$   $\mu\text{s}$  relative to event triggers, measured with  
 563 an Am/Be neutron source positioned near the ID tank cen-  
 564 ter. The black points represent SK-VI data, while the red  
 565 line shows the simulated prediction. The green dashed ar-  
 566 rows indicate the selection window for 4.44 MeV gamma-ray-  
 567 induced scintillation. Roughly 95% of the selected events are  
 568 attributed to gamma-rays from the Am/Be source (green),  
 569 with the remaining 5% arising from ambient neutron cap-  
 570 tures (blue) and neutrons inelastically producing charged par-  
 571 ticles in the scintillator (orange). The contribution from back-  
 572 ground events (labeled “BG,” gray) is negligible.



573 FIG. 9. Exponential decrease of the selected neutron signal  
 574 candidates as a function of the time from the selected event  
 575 triggers with the Am/Be neutron source positioned near the  
 576 ID tank center, in the SK-VI phase. The label “Trigger ( $n, \gamma$ )”  
 577 indicates captures of neutrons that are produced within 350  
 578 ns from the event trigger, while the label “Pile-up ( $n, \gamma$ )”  
 579 indicates captures of piled-up neutrons without such corre-  
 580 lation to the event trigger.

581 Figure 9 shows an example time distribution of the  
 582 selected signal candidates. Such distributions of the time  
 583  $t$  were fitted with a function  $f$  of the form:

$$f(t) = A(1 - e^{-t/\tau_{\text{thermal}}})e^{-t/\tau_{\text{capture}}} + B \quad (3)$$

584 where the normalization constant  $A$ , the background  
 585 constant  $B$ , the neutron thermalization time scale  
 586  $\tau_{\text{thermal}}$ , and the neutron capture time constant  $\tau_{\text{capture}}$   
 587 are free parameters. The signal efficiency was evaluated  
 588 as the number of identified signals per selected event trig-  
 589 gers, corrected by the constant background term  $B$ . Figure  
 590 10 shows the estimated neutron detection efficiencies  
 591 for various source positions in the ID.

592 The major sources of systematic uncertainty are sum-  
 593 marized in Table II. In the pure water phases (SK-IV  
 594 and V), the dominant source of uncertainty lies in the  
 595 potential bias caused by the calibration setup, such as  
 596 the unwanted event triggers or time correlation of false  
 597 positives to event triggers, often leading to an overesti-  
 598 mation of the background constant  $B$ . The size of this  
 599 uncertainty was conservatively estimated by comparing  
 600 the true and estimated signal efficiencies from the sim-  
 601 ulations and quantifying the fluctuation within each SK  
 602 phase. In the Gd-loaded phase (SK-VI), the dominant  
 603 source of uncertainty is in the fraction and the  $\gamma$  emis-  
 604 sion model of the  $Gd(n, \gamma)$  reaction. The size of these un-  
 605 certainties is estimated based on the evaluated thermal  
 606 neutron capture cross-section uncertainties in ENDF/B-  
 607 VII.1, as well as variations in the estimated signal effi-  
 608 ciency when using an alternative photon strength func-  
 609 tion to describe the Gd continuum gamma cascade in the  
 610 ANNRI-Gd model [41].

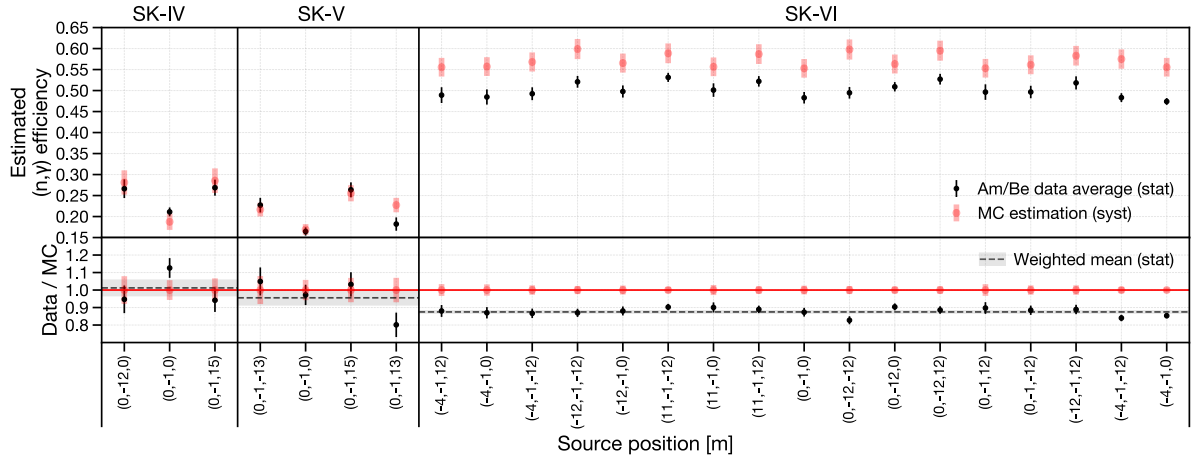


FIG. 10. Estimated  $(n, \gamma)$  signal selection efficiency for each calibration position within the tank. For positions in SK-VI where there are multiple measurements at different dates, the estimated efficiencies were averaged. The systematic uncertainties considered for MC simulation are summarized in Table II.

TABLE II. Major sources of systematic uncertainty in the neutron detection efficiency estimated with the Am/Be neutron source.

Source	SK-IV	SK-V	SK-VI
Am/Be neutron characterization	0.5%	0.9%	0.5%
Detector response	2.2%	3.3%	1.2%
Bias due to calibration setup	6.9%	4.6%	1.1%
Gd( $n, \gamma$ ) fraction	-	-	2.1%
Gd( $n, \gamma$ ) $\gamma$ emission model	-	-	2.6%
Total	7.3%	5.7%	3.8%

The noticeable difference between the observed and predicted signal efficiencies in SK-VI is thought to stem from the overestimation of the Gd( $n, \gamma$ ) fraction in our MC simulation setup. Figure 11 compares the MC-simulated Gd( $n, \gamma$ ) fraction  $r_{\text{Gd}}$  with the analytically evaluated fraction, assuming completely thermalized neutrons:

$$r_{\text{Gd}} \approx 1 - r_{\text{H}} \approx 1 - \frac{n_{\text{H}} g_{\text{H}}(T) \sigma_{\text{H}}(v_{\text{thermal}})}{\sum_i n_i g_i(T) \sigma_i(v_{\text{thermal}})} \quad (4)$$

Here, for the  $i^{\text{th}}$  isotope,  $n_i$  is the number density,  $g_i(T)$  is the Westcott  $g$ -factor for temperature  $T$ , and  $\sigma_i(v_{\text{thermal}})$  is the neutron capture cross section evaluated at thermal neutron speed  $v_{\text{thermal}} = 2200$  m/s.

The value estimated with SK-VI Am/Be data agrees well with the analytical evaluation based on  $g_i$  and  $\sigma_i$  from ENDF/B-VII.1 [51], while both differ from the MC simulation using Geant4.10.05.p01 NeutronHP and ENDF/B-VII.1. The reason seems to be that the NeutronHP model considers the thermal motion of hydrogen as free rather than bound in a water molecule [52], thus underestimating the fraction of  ${}^1\text{H}(n, \gamma)$  that competes with the Gd( $n, \gamma$ ) reaction.

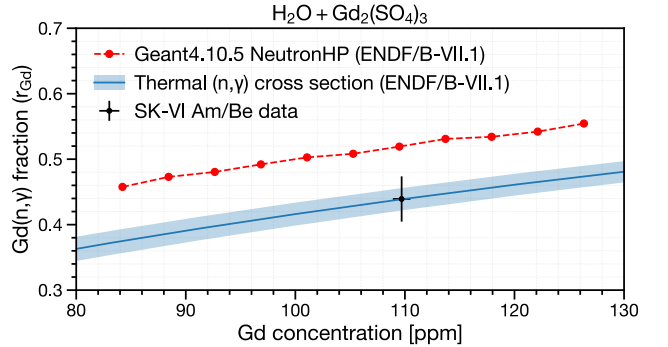


FIG. 11. Predicted Gd( $n, \gamma$ ) fraction in Gd-loaded water as a function of Gd concentration, compared with SK-VI Am/Be data (black). The red dots represent predictions by MC simulation using the NeutronHP model in Geant4.10.05.p01 with neutron cross sections from ENDF/B-VII.1, while the blue line and shades represent evaluation of Equation 4 based on the evaluated thermal ( $n, \gamma$ ) cross sections and uncertainties in ENDF/B-VII.1.

To account for such a difference between signal efficiencies evaluated with Am/Be data and MC simulation, we used the weighted mean of the ratios of the two evaluated at all Am/Be source positions as the correction factor. The obtained efficiency correction factor was  $1.01 \pm 0.04$  for SK-IV,  $0.96 \pm 0.04$  for SK-V, and  $0.88 \pm 0.01$  for SK-VI, including both statistical and systematic errors.

The average neutron capture time constants were measured as  $200.4 \pm 3.7$   $\mu\text{s}$  for the pure water phase (SK-IV, V) and  $116.9 \pm 0.3$   $\mu\text{s}$  for the Gd-loaded phase (SK-VI). These results are consistent with ENDF/B-VII.1 predictions of  $204.7 \pm 5.3$   $\mu\text{s}$  and  $114.9 \pm 2.5$   $\mu\text{s}$ , where the errors are derived from evaluated cross section uncertainties. Relative to this, the Geant4 prediction for the Gd-loaded phase was  $112.4$   $\mu\text{s}$ .

## 609 V. $(n, \gamma)$ MULTIPLICITY ESTIMATION

610 The average multiplicity of  $(n, \gamma)$  reactions, or neutrino captures, is computed as the average of the expected number of  $(n, \gamma)$  reactions estimated on an event-by-event basis, as follows:

611  
612  
613  
614  
615  
616  
617  
618  
619  
620  
621  
622  
623  
624  
625  
626  
627  
628  
629  
630  
631  
632  
633

$$634 \quad \langle N \rangle = \left\langle \frac{N_i^{\text{detected}} - N_i^{\text{BG}}}{\epsilon_i} \right\rangle \quad 635 \quad (5) \quad 636 \quad 637 \quad 638 \quad 639 \quad 640 \quad 641 \quad 642 \quad 643 \quad 644$$

645 Here,  $N_i^{\text{detected}}$  is the count of detected signals,  $N_i^{\text{BG}}$  is the estimated number of false positives, and  $\epsilon_i$  is the estimated signal detection efficiency of the  $i^{\text{th}}$  event.

646 Accurate estimation of  $N_i^{\text{BG}}$  and  $\epsilon_i$  is crucial. While Am/Be calibration data provides a basis for these estimates, additional factors in atmospheric neutrino events—such as neutrino vertex reconstruction accuracy and larger neutron kinetic energy—may significantly impact the performance of signal selection. To better account for these effects in the calculation of  $N_i^{\text{BG}}$  and  $\epsilon_i$ , we trained Generalized Additive Models (GAMs) [53] on default atmospheric neutrino event simulations. A total of six GAMs were constructed across the three SK phases, for two output metrics: signal efficiency and false positive rate, using the `LinearGAM` class in pyGAM 0.9.0 [54].

647 The following major systematic uncertainties affecting signal counting were evaluated on a bin-by-bin basis:

### (1) Overall signal efficiency scale

648 This includes uncertainties in calibrated efficiency correction factors, as well as neutron momentum and detector modeling, which are accounted for by comparing the results across different SK phases as described in Section VII.

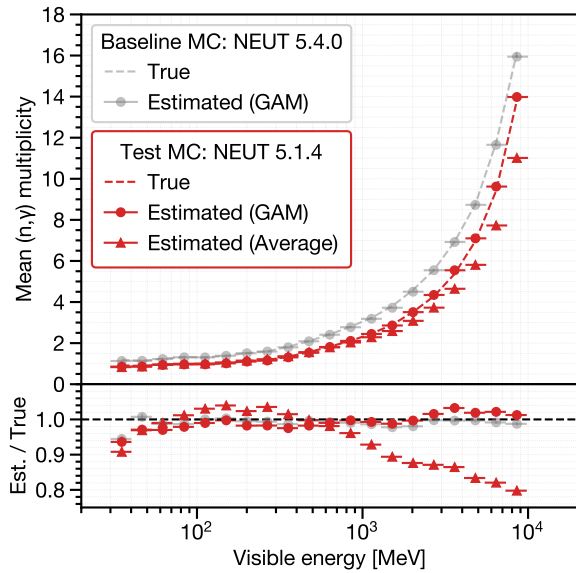
### (2) Signal selection performance modeling (GAM)

649 This refers to potential errors in the regression model used to describe the signal selection performance for atmospheric neutrino events. The uncertainty is quantified as the difference between the true and estimated signal multiplicity in a test simulation setup, as shown in Figure 12.

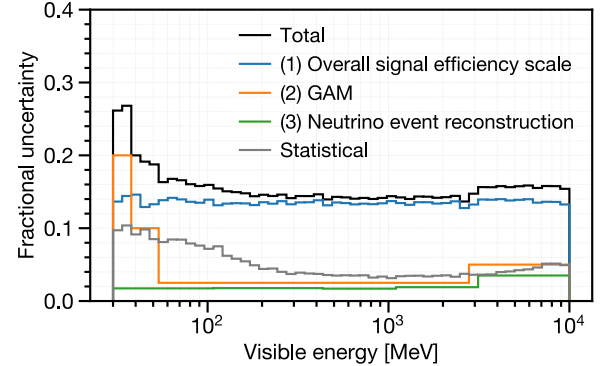
### (3) Neutrino event reconstruction

650 This assumes a uniform 2% visible energy resolution, as described in Sec. II and Figure 2.

651 Figure 13 illustrates the distribution of fractional uncertainties assigned to each visible energy bin. The most dominant factor is the overall signal efficiency scale.



652 FIG. 12. Comparison of the true (dashed lines) and estimated (circle markers: using GAM, triangle markers: using the overall average signal efficiency and false positive rate) average  $(n, \gamma)$  multiplicity as a function of visible energy, for both baseline and test simulations of atmospheric neutrino events.



653 FIG. 13. Fractional uncertainties assigned to the estimated average  $(n, \gamma)$  multiplicity on a bin-by-bin basis.

## VI. TESTED INTERACTION MODELS

To compare with the data, we generated predictions for the average  $(n, \gamma)$  multiplicity as a function of neutrino event visible energy using 30 different test configurations of neutrino event generators and secondary hadron-nucleus interaction models. Six different setups of neutrino event generators were tested: NEUT 5.4.0, NEUT 5.6.3, and GENIE 3.4.0 with G\_18a\_10x\_02\_11b physics tunes [20], where  $x \in \{a, b, c, d\}$ . Here, a, b, c, and d represent the use of INTRANUKE/hA, hN [19], the Liège INC model [55] (INCL++), and the Geant4 Bertini cascade model [56] (G4Bertini) for FSI modeling, respectively. NEUT 5.4.0 was implemented as described in Section III C, while NEUT 5.6.3 employed the same interaction models but with a modified nuclear binding energy, resulting in a slightly reduced fraction of CCQE interactions. GENIE 3.4.0 with the specified physics tunes employed similar models for QE and single-pion production as the NEUT versions but featured different FSI and final-state hadronization models. All FSI models except the GENIE “hA” model are full INC models based on free nucleon cross sections. INCL++ was coupled with ABLA07 [57] to model nuclear de-excitation. Figure 14 presents the outgoing neutron momentum distributions for various tested neutrino event generator setups.

Models for secondary hadron-nucleus interactions were also varied using the SK detector simulation software, based on Geant3.21 and Geant4.10.05.p01. Five detector simulation configurations were tested: SK-IV/V default, SK-VI default, GCALOR, BERT\_HP, and the Liège INC model [55] (INCLXX\_HP). The SK-IV/V and SK-VI defaults differ primarily in their use of MICAP (based on ENDF/B-V) or NeutronHP (based on ENDF/B-VII.1) for low-energy neutron propagation below 20 MeV. GCALOR, which features its own hadron propagation routine for pions, contrasts with the baseline setups that use the NEUT pion FSI routine. The BERT\_HP and INCLXX\_HP configurations, implemented in Geant4.10.05.p01, were paired with NeutronHP for low-energy neutron propagation. Additionally, INCLXX\_HP was coupled with the Geant4 Pre-compound and Evaporation models [58] for nuclear de-excitation. Figure 15 compares the average signal multiplicity as a function of projectile neutron momentum for various configurations of secondary interaction models. Notably, the outgoing neutron momentum distributions show significant variation among the generator setups, and the INCLXX\_HP as secondary interaction model predicts  $\sim 30\%$  lower average  $(n, \gamma)$  multiplicities. The underlying physics responsible for these differences in model predictions is discussed in Section VIII.

For each neutrino event generator, a full MC simulation equivalent to 50 years of atmospheric neutrino observation was generated using the baseline detector model (SK-VI default). To account for variations in secondary interactions without additional full simulations, we tabulated average signal multiplicities for projectile hadrons

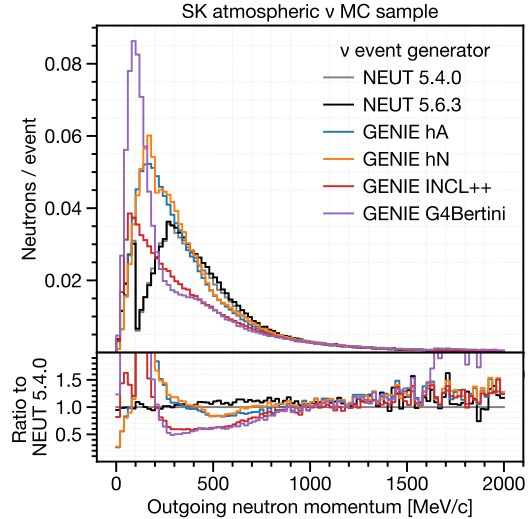


FIG. 14. Model comparison: Outgoing neutron momentum distribution per selected atmospheric neutrino event.

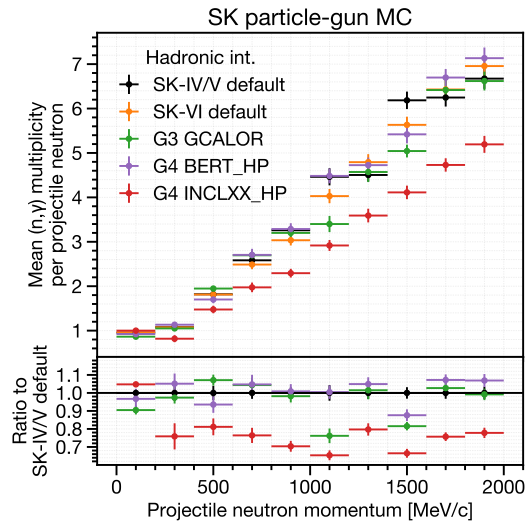


FIG. 15. Model comparison: Average  $(n, \gamma)$  multiplicity per projectile neutron momentum bin, based on simulations using a single-neutron particle-gun setup in water.

$(n, p, \pi^\pm, \text{ and } \mu^-)$  in water up to 10 GeV/c, based on particle-gun MC simulations. Figure 15 shows an example for neutrons.

Predictions were made by convolving hadron momentum distributions with the momentum-to-multiplicity tables. For each event generator, ratios relative to the baseline detector simulation model (SK-VI default) were applied to scale the signal multiplicities obtained from the full MC simulation. For the two NEUT options coupled with the “SK-IV/V default” model, the discrepancy compared to the full MC simulation was within 15% for bins below 100 MeV and within 5% for bins above 100 MeV.

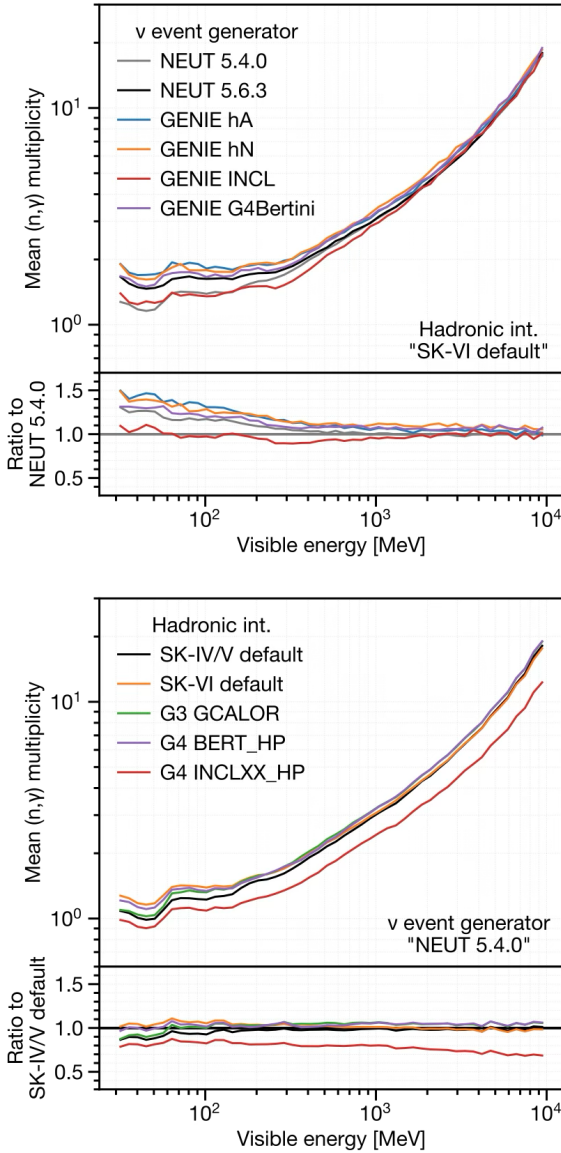


FIG. 16. Comparison of the neutrino event generator options (top) and detector simulator options (bottom) on the predicted average  $(n, \gamma)$  multiplicity. In the top figure, each neutrino event generator option is paired with the baseline secondary interaction model (SK-VI default). In the bottom figure, each detector simulator option is paired with the baseline neutrino event generator option (NEUT 5.4.0).

Figure 16 breaks down the overall model prediction variability into two sources. Prediction variability across different neutrino event generator configurations is more prominent at lower energies, while variability within detector simulator configurations dominates at higher energies. As mentioned earlier, INCL resulted in the least neutron production, both when used in the neutrino event generator (coupled with ABLA07) and in the detector simulator (coupled with the Geant4 Precompound model).

## VII. RESULTS

Table III summarizes the number of atmospheric neutrino events (“ $\nu$  events”) and detected neutron signals (“ $n$  signals”) in the final data sample. The differences in  $\langle N \rangle_{\text{total}}$  are primarily due to uncertainty in the signal efficiency scale.

TABLE III. Summary of atmospheric neutrino events and detected neutron signals in the final data sample.  $\langle N \rangle_{\text{total}}$  denotes the average  $(n, \gamma)$  multiplicity and its systematic uncertainty. Other errors shown are purely statistical.

	SK-IV	SK-V	SK-VI
$\nu$ events	29,942	4,231	5,203
Events/day	$9.23 \pm 0.05$	$9.18 \pm 0.14$	$9.22 \pm 0.13$
$n$ signals	15,705	2,035	5,752
$n$ signals/event	$0.525 \pm 0.004$	$0.481 \pm 0.011$	$1.106 \pm 0.015$
$\langle N \rangle_{\text{total}}$	$2.04 \pm 0.34$	$2.33 \pm 0.27$	$2.36 \pm 0.21$

Figure 17 compares the estimated average  $(n, \gamma)$  multiplicity per visible energy bin across SK phases. To account for uncertainties in outgoing neutron kinematics that affect signal detection efficiency, an independent algorithm using a likelihood fitter [59] was applied to SK-VI data to reconstruct the  $Gd(n, \gamma)$  vertex, providing a reference for the results in Table III. The scale differences between SK phases and the reference are included as systematic uncertainties in the signal efficiency scale, as shown in Table III and Figure 13.

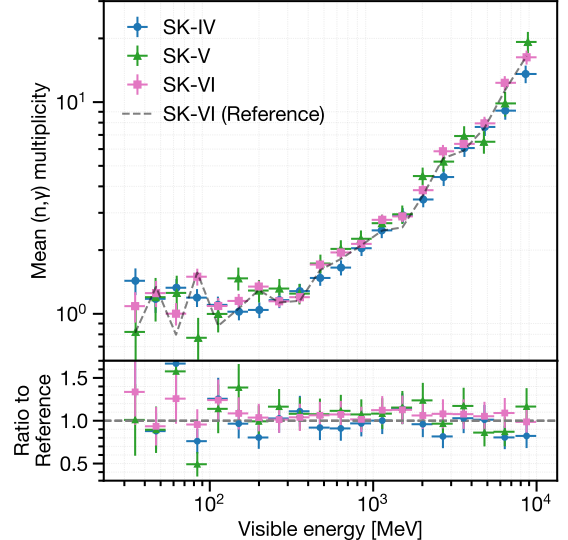


FIG. 17. Comparison of average  $(n, \gamma)$  multiplicity across SK phases, with error bars representing both statistical and systematic uncertainties. The dashed line labeled “SK-VI (Reference)” shows the result from SK-VI data using a reference algorithm whose performance is largely independent of neutron kinetic energy.

766 The combined data estimate was compared with the  
 767 SK-VI MC simulation and neutron production estimates  
 768 in water from SNO [7], as shown in Figure 18. While  
 769 the combined data estimate aligned well with the SNO  
 770 estimate, it was 20-40% lower than the SK-VI simulation  
 771 results across different energy ranges.

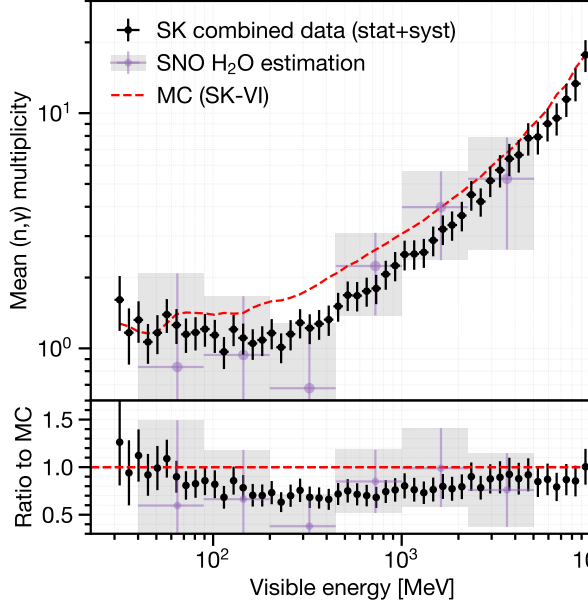


FIG. 18. Average  $(n, \gamma)$  multiplicity estimated for atmospheric neutrino interactions versus visible energy. The black dots and error bars represent combined SK data, including statistical and systematic uncertainties. Purple crosses with shading indicate estimates of neutron production in water derived from SNO measurements using a D<sub>2</sub>O target volume [7]. The red dashed line represents the true average  $(n, \gamma)$  multiplicity per visible energy bin obtained from SK-IV MC simulation.

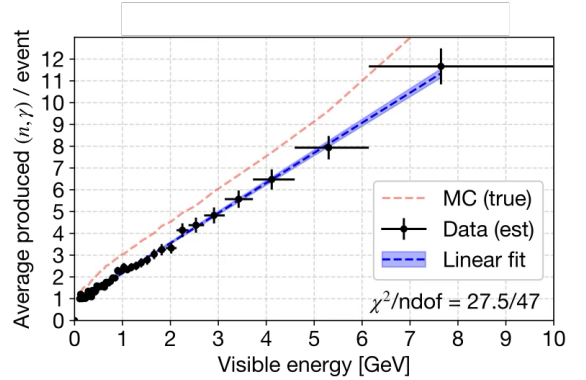


FIG. 19. Average  $(n, \gamma)$  multiplicity versus visible energy, with vertical axis in linear scale (same data as in Figure 18 with a different binning scheme). The error bars include both statistical and systematic errors. The shaded area represents the standard errors associated with the linear fit. The label ‘MC’ denotes the SK-IV simulation.

789 both the observed slopes and intercepts were notably  
 790 smaller than those expected from the MC simulation.

### A. Linearity

772  
 773 We observed a linear relationship between the average  
 774  $(n, \gamma)$  multiplicity and the visible energy of each neu-  
 775 trino event, as shown in Figure 19. This relationship was  
 776 modeled using a function of the form  $y = ax + b$ , where  $x$   
 777 represents the average visible energy in each bin,  $y$  stands  
 778 for the average  $(n, \gamma)$  multiplicity, and  $a$  and  $b$  denote the  
 779 slope and intercept, respectively, as free parameters. The  
 780 dataset was categorized by SK phases as well as single-  
 781 ring and multi-ring events.

782 Figure ?? shows fit consistency across different SK  
 783 phases. Both the slopes and intercepts were greater in  
 784 multi-ring events compared to single-ring events, as ex-  
 785 pected from the SK-IV MC simulation. This aligns with  
 786 the notion that multi-ring events are more frequently  
 787 caused by DIS events, resulting in higher energy transfer  
 788 to the hadron system, as shown in Figure 5. However,

## 791 B. Comparison with model predictions

792 Predictions from various model combinations, as de-  
 793 scribed in Section VI, were compared with the combined  
 794 data results, as shown in Figure 20. Compared to the  
 795 default SK-VI simulation setup, represented by the red  
 796 dashed line, the data showed a 20-40% deficit, partic-  
 797 ularly in the  $O(1)$  GeV visible energy range. Varying  
 798 neutrino event generator options, which mainly affect the  
 799 outgoing hadron kinematics from the target nucleus as il-  
 800 lustrated in Figure 14, resulted in a 5-15% change in the  
 801 overall prediction. However, the combined data estima-  
 802 tion was clearly inconsistent with the prediction range of  
 803 the various neutrino event generator options. Changing  
 804 the secondary spallation model option had a more signif-  
 805 icant impact, causing a -20% to +20% difference in the  
 806 overall prediction compared to the default setup.

807 The secondary spallation model with the smallest pre-  
 808 diction was INCLXX\_HP, and its combination with the  
 809 default neutrino event generator option NEUT 5.4.0  
 810 showed the best agreement with our data. This is ev-  
 811 ident when comparing the fitted slopes and intercepts  
 812 of each model combination’s predictions with those of  
 813 the combined data, as illustrated in Figure 22. There  
 814 was a clear distinction in the fitted slopes between IN-  
 815 CLXX\_HP and the other secondary interaction options,  
 816 especially in multi-ring events with larger hadron pro-  
 817 duction. There was also a slight variation in the fitted  
 818 intercepts among different event generator options, with  
 819 NEUT and GENIE 3.4.0 combined with the INCL++  
 820 option aligning better with the data.

## 821 VIII. DISCUSSION

822 Figure 21 shows that with higher visible energy, neu-  
 823 trons produced through hadronic secondary interactions  
 824 in water predominate so that the linear slope is directly  
 825 related to the secondary interaction model. The observed  
 826 slope provides model discriminant power, as indicated by  
 827 the separation between INCLXX\_HP and other models  
 828 in Figure 22. Figure 14 offers insights into the potential  
 829 reasons for the variations in predictions of hadronic in-  
 830 teraction models. For example, comparing the outgoing  
 831 neutron momentum distribution between the two GENIE  
 832 FSI options, INCL++ and G4Bertini, suggests that the  
 833 difference in slopes between INCLXX\_HP and the other  
 834 models is largely due to neutrons below Fermi momen-  
 835 tum produced through the de-excitation process.

836 Additionally, different cascade stopping criteria can re-  
 837 sult in different residual energies left for de-excitation,  
 838 leading to varying nucleon emission rates. The Liège  
 839 model’s consideration of cluster formation among out-  
 840 going nucleons near the nuclear surface is also expected  
 841 to reduce the number of outgoing neutrons [60]. Our  
 842 results highlight the importance of accurately modeling  
 843 secondary hadronic interactions to predict neutron cap-  
 844 ture multiplicity in neutrino events.

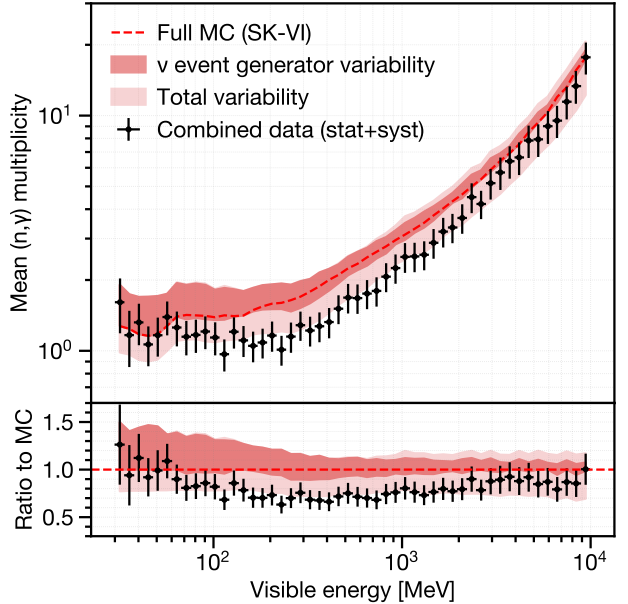


FIG. 20. Comparison of various model predictions with the combined data, showing average  $(n, \gamma)$  multiplicity as a function of atmospheric neutrino event visible energy. The black dots with error bars represent the combined data results, including statistical and systematic uncertainties. The dashed red line represents the prediction from the full SK-VI MC simulation using the default setup. The thick red shaded area shows the range of predictions when varying the neutrino event generator options, while keeping the secondary spallation model fixed to the SK-VI default. The light red shaded area shows the range of predictions from all tested model combinations.

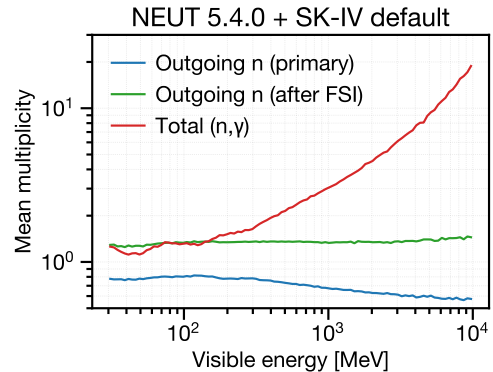


FIG. 21. Average multiplicity of outgoing neutrons and resulting  $(n, \gamma)$  reactions as a function of visible energy, based on predictions from the baseline SK-IV simulation setup. The blue and green lines indicate the number of neutrons produced at the nucleon level (blue) and after FSI (green), as modeled by NEUT 5.4.0. The red line represents the average total  $(n, \gamma)$  reactions per bin, including the effects of secondary hadronic interactions.

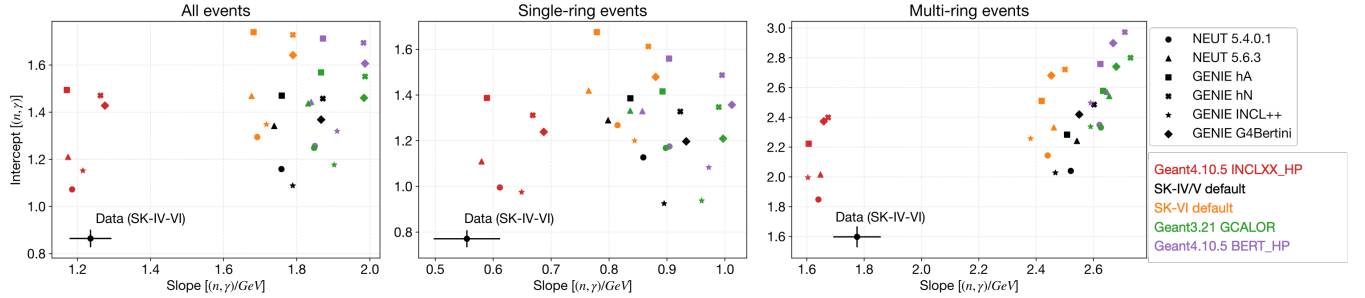


FIG. 22. Scatter plots of fitted slopes and intercepts in model predictions and data (black circles with error bars), shown for all events (left), single-ring events (middle), and multi-ring events (right). Different shapes represent various neutrino event generator options, while different colors indicate the secondary hadron-nucleus interaction model options used.

845 The fitted intercept is expected to be more dependent on the neutrino event generator option, as indicated in Figure 21. Regarding differences among neutrino event generator options, Pauli blocking implementation appears to be a significant factor. NEUT strictly blocks all nucleon ejection below oxygen Fermi momentum, resulting in a large dip in the outgoing neutron momentum distribution near Fermi momentum, while GENIE native hN and hA do not consider Pauli blocking. The Liège model uses probabilistic Pauli blocking, considering nucleon holes. Additionally, INCL++ and G4Bertini, with medium corrections such as nucleon repulsion and correlations of nucleon interactions, predict much lower neutron production at medium energies compared to other options. In contrast, variations in pion-nucleus interaction models (e.g., NEUT’s low-energy pion FSI model in the “SK-IV/V default” model and the Bertini cascade model in the “GCALOR” model) or low-energy neutron-reaction cross-section datasets (e.g., ENDF/B-V cross sections in the “SK-IV/V default” model and ENDF/B-VII.1 in the “SK-VI default” model) seem to have a relatively small effect.

856 The largest difference among neutrino event generator predictions below 100 MeV visible energy is about 30% between GENIE hA/hN and NEUT 5.4.0 predictions with the same secondary hadron-nucleus interaction model. FSI models with lower neutron production are preferred, while these model differences at the lower energy end are comparable to our current systematic uncertainty estimate.

In this paper, we present the measurement of total neutron production following atmospheric neutrino interactions within the Super-Kamiokande (SK) detector’s water volume. In SK, neutrons with kinetic energies below a few MeV are typically captured by surrounding nuclei, such as  $^1\text{H}$  or  $^{155}/^{157}\text{Gd}$ , radiating 2-8 MeV of energy through gamma-rays. We used a neutron capture detection algorithm based on a simple low-energy trigger and a neural network binary classification, calibrated with an Am/Be neutron source. Neutron capture multiplicity was estimated on an event-by-event basis using a multivariate non-linear regression technique. Atmospheric neutrino events were binned by their electron-equivalent “visible energy,” which is a semi-calorimetric measure of the neutrino momentum transfer. The average neutron capture multiplicity per visible energy bin was then compared with predictions from various combinations of neutrino event generator options and secondary hadron-nucleus interaction models.

For this study, we utilized the largest dataset of neutrino events in water, covering the widest visible energy range from 30 MeV to 10 GeV. This extensive dataset provides significant discriminative power for hadron-nucleus interaction models. With reduced uncertainties, we quantified the linearity in observed average neutron capture multiplicity versus visible energy. The observed differential increase of the average signal multiplicity per visible energy was larger with multi-ring events, characterized by a higher fraction of inelastic interactions, compared to single-ring events.

We also evaluated the performance of the Liège model (INCL++), which includes several low-energy corrections and has shown good agreement with measurements within INC energy limits, as an alternative to the Bertini model. While a neutron deficit was observed compared to predictions using the Bertini cascade model and its variants for secondary hadron-nucleus interactions, better agreement was achieved with the Liège cascade model for intranuclear hadron transport, coupled with the Geant4 Precompound and Evaporation models for nuclear de-excitation. This combination predicted significantly fewer neutrons below the oxygen Fermi momen-

## IX. SUMMARY

876 Accurately modeling neutron production in neutrino interactions is essential for characterizing incoming neutrinos, which is crucial for advancing precision measurements of neutrino oscillation parameters and rare event searches involving neutron tagging. Recent studies have suggested potential inaccuracies in the widely used Bertini cascade model for describing secondary hadron-nucleus interactions.

926 tum compared to the Bertini model. This highlights the  
 927 importance of the accuracy of secondary hadron-nucleus  
 928 interaction models in predicting neutron capture multi-  
 929 plicity in neutrino events.

930 **ACKNOWLEDGMENTS**

931 We gratefully acknowledge the cooperation of the  
 932 Kamioka Mining and Smelting Company. The Super-  
 933 Kamiokande experiment has been built and operated  
 934 from funding by the Japanese Ministry of Education,  
 935 Culture, Sports, Science and Technology, the U.S. De-  
 936 partment of Energy, and the U.S. National Science Foun-  
 937 dation. Some of us have been supported by funds from  
 938 the National Research Foundation of Korea NRF-2009-  
 939 0083526 (KNRC) funded by the Ministry of Science,  
 940 ICT, and Future Planning and the Ministry of Educa-  
 941 tion (2018R1D1A1B07049158, 2021R1I1A1A01059559),  
 942 the Japan Society for the Promotion of Science, the  
 943 National Natural Science Foundation of China under  
 944 Grants No.11620101004, the Spanish Ministry of Science,  
 945 Universities and Innovation (grant PGC2018-099388-B-  
 946 I00), the Natural Sciences and Engineering Research  
 947 Council (NSERC) of Canada, the Scinet and West-  
 948 grid consortia of Compute Canada, the National Sci-  
 949 ence Centre (UMO-2018/30/E/ST2/00441) and the Min-  
 950 istry of Education and Science (DIR/WK/2017/05),  
 951 Poland, the Science and Technology Facilities Council  
 952 (STFC) and GridPPP, UK, the European Union's Horiz-  
 953 on 2020 Research and Innovation Programme under  
 954 the Marie Skłodowska-Curie grant agreement no.754496,  
 955 H2020-MSCA-RISE-2018 JENNIFER2 grant agreement  
 956 no.822070, and H2020-MSCA-RISE-2019 SK2HK grant  
 957 agreement no. 872549.

- [1] P. Abratenko *et al.* (MicroBooNE collaboration), Phys. Rev. D **110**, 013006 (2024).  
[2] P. Abratenko *et al.* (MicroBooNE collaboration), The European Physical Journal C **84**, 1052 (2024).  
[3] A. M. Ankowski, P. Coloma, P. Huber, C. Mariani, and E. Vagnoni, Phys. Rev. D **92**, 091301 (2015).  
[4] T. Wester *et al.* (Super-Kamiokande collaboration), Phys. Rev. D **109**, 072014 (2024).  
[5] A. Takenaka *et al.* (Super-Kamiokande collaboration), Phys. Rev. D **102**, 112011 (2020).  
[6] R. Akutsu, A study of neutrons associated with neutrino and antineutrino interactions on the water target at the T2K far detector, Ph.D. thesis, The Univ. of Tokyo (2019).  
[7] B. Aharmim *et al.* (SNO collaboration), Phys. Rev. D **99**, 112007 (2019).  
[8] M. Elkins *et al.* (MINERvA collaboration), Phys. Rev. D **100**, 052002 (2019).  
[9] A. Olivier *et al.* (MINERvA collaboration), Phys. Rev. D **108**, 112010 (2023).  
[10] J. Cugnon, Nucl. Phys. A **387**, 191 (1982).  
[11] J.-C. David, D. Filges, F. Gallmeier, M. Khandaker, A. Konobeyev, S. Leray, G. Mank, A. Mengoni, R. Michel, N. Otsuka, and Y. Yariv, Progress In Nuclear Science and Technology **2**, 942 (2011).  
[12] M. B. Chadwick *et al.*, Nuclear Data Sheets **112**, 2887 (2011), special Issue on ENDF/B-VII.1 Library.  
[13] K. Abe *et al.* (Super-Kamiokande collaboration), Nucl. Instrum. Methods A **1027**, 166248 (2022).  
[14] K. Abe *et al.*, Nuclear Instruments and Methods in Physics Research Section A: Accelerators, Spectrometers, Detectors and Associated Equipment **1065**, 169480 (2024).  
[15] S. Fukuda *et al.* (Super-Kamiokande collaboration), Nucl. Instrum. Methods A **501**, 418 (2003).  
[16] K. Abe *et al.*, Nucl. Instrum. Methods A **737**, 253–272 (2014).  
[17] S. Yamada, K. Awai, Y. Hayato, K. Kaneyuki, Y. Kouzuma, S. Nakayama, H. Nishino, K. Okumura, Y. Obayashi, Y. Shimizu, *et al.*, IEEE Trans. Nucl. Sci. **57**, 428 (2010).  
[18] C. Andreopoulos *et al.*, Nucl. Instrum. Methods A **614**, 87 (2010), arXiv:0905.2517 [hep-ph].  
[19] C. Andreopoulos, C. Barry, S. Dytman, H. Gallagher, T. Golan, R. Hatcher, G. Perdue, and J. Yarba, The GENIE Neutrino Monte Carlo Generator: Physics and User Manual (2015), arXiv:1510.05494 [hep-ph].  
[20] J. Tena-Vidal *et al.* (GENIE), Phys. Rev. D **104**, 072009 (2021), arXiv:2104.09179 [hep-ph].  
[21] M. Shiozawa, Nucl. Instrum. Methods A **433**, 240 (1999).  
[22] M. Honda, T. Kajita, K. Kasahara, and S. Midorikawa, Phys. Rev. D **83**, 123001 (2011).  
[23] R. L. Workman *et al.* (Particle Data Group), PTEP **2022**, 083C01 (2022).  
[24] Y. Hayato and L. Pickering, Eur. Phys. J Spec. Top. **230**, 4469–4481 (2021).  
[25] L. L. Salcedo, E. Oset, M. J. Vicente-Vacas, and C. Garcia-Recio, Nucl. Phys. A **484**, 557 (1988).  
[26] E. S. P. Guerra *et al.*, Phys. Rev. D **99**, 052007 (2019).  
[27] H. W. Bertini, Phys. Rev. **131**, 1801 (1963).  
[28] P. de Perio, AIP Conf. Proc. **1405**, 223 (2011), arXiv:1405.3973 [nucl-ex].  
[29] A. M. Ankowski, O. Benhar, T. Mori, R. Yamaguchi, and M. Sakuda, Phys. Rev. Lett. **108**, 052505 (2012).  
[30] H. Ejiri, Phys. Rev. C **48**, 1442 (1993).  
[31] R. Brun, F. Bruyant, M. Maire, A. C. McPherson, and P. Zanarini, GEANT3, Tech. Rep. (1987).  
[32] A. Ferrari, P. R. Sala, A. Fasso, and J. Ranft, FLUKA: A multi-particle transport code (Program version 2005), Tech. Rep. (2005).  
[33] H. W. Bertini, Phys. Rev. **188**, 1711 (1969).  
[34] W. A. Coleman and T. W. Armstrong, NUCLEON-MESON TRANSPORT CODE NMTC., Tech. Rep. (Oak Ridge National Laboratory, Oak Ridge, TN, USA, 1970).  
[35] T. A. Gabriel, J. O. Johnson, and J. Brau, MICAP: A program for low energy neutron, ion and gamma-ray transport and one of its applications in calorimeter design, Tech. Rep. (United States, 1987) cONF-8708186-7.  
[36] C. S. E. W. Group, ENDF/B summary documentation, Tech. Rep. BNL-NCS-1754 (ENDF-201) (National Nuclear Data Center, Brookhaven National Laboratory, Upton, NY, USA, 1979).  
[37] S. Agostinelli *et al.* (Geant4 collaboration), Nucl. Instrum. Methods A **506**, 250 (2003).  
[38] J. Allison *et al.*, IEEE Transactions on Nuclear Science **53**, 270 (2006).  
[39] J. Allison *et al.*, Nucl. Instrum. Methods A **835**, 186 (2016).  
[40] E. Mendoza and D. Cano-Ott, Update of the Evaluated Neutron Cross Section Libraries for the Geant4 Code (see also INDC(NDS)-0612), Tech. Rep. (International Atomic Energy Agency (IAEA), 2018) iNDc(NDS)-0758.  
[41] K. Hagiwara *et al.*, Prog. Theor. Exp. Phys. **2019**, 023D01 (2019), <https://academic.oup.com/ptep/article-pdf/2019/2/023D01/27970473/ptz002.pdf>.  
[42] T. Tanaka *et al.*, Prog. Theor. Exp. Phys. **2020**, 043D02 (2020), <https://academic.oup.com/ptep/article-pdf/2020/4/043D02/33040537/ptaa015.pdf>.  
[43] V. Barger, K. Whisnant, S. Pakvasa, and R. J. N. Phillips, Phys. Rev. D **22**, 2718 (1980).  
[44] M. Jiang *et al.* (Super-Kamiokande collaboration), Progress of Theoretical and Experimental Physics **2019**, 053F01 (2019), <https://academic.oup.com/ptep/article-pdf/2019/5/053F01/28638877/ptz015.pdf>.  
[45] A. M. Dziewonski and D. L. Anderson, Physics of the Earth and Planetary Interiors **25**, 297 (1981).  
[46] K. Abe *et al.* (Super-Kamiokande collaboration), J. Instrum. **17** (10), P10029.  
[47] F. Chollet *et al.*, Keras, <https://keras.io> (2015).  
[48] K. He, X. Zhang, S. Ren, and J. Sun, Delving deep into rectifiers: Surpassing human-level performance on imagenet classification (2015), arXiv:1502.01852 [cs.CV].  
[49] D. P. Kingma and J. Ba, Adam: A method for stochastic optimization (2017), arXiv:1412.6980 [cs.LG].  
[50] H. Ito, K. Wada, T. Yano, Y. Hino, Y. Ommura, M. Harada, A. Minamino, and M. Ishitsuka, Nucl. Instrum. Methods A **1057**, 168701 (2023).  
[51] B. Pritychenko and S. F. Mughabghab, Nuclear Data Sheets **113**, 3120 (2012).  
[52] Y. Hino, K. Abe, R. Asaka, S. Han, M. Harada, M. Ishitsuka, H. Ito, S. Izumiya, Y. Kanemura, Y. Koshio,

- 1080 F. Nakanishi, H. Sekiya, and T. Yano, Modification on<sup>1092</sup>  
 1081 thermal motion in geant4 for neutron capture simula<sup>1093</sup>  
 1082 tion in gadolinium loaded water (2024), arXiv:2412.04186<sup>1094</sup>  
 1083 [hep-ex].<sup>1095</sup>
- 1084 [53] T. Hastie and R. Tibshirani, *Generalized Additive Mod<sup>1096</sup>*, Chapman & Hall/CRC Monographs on Statistics &<sup>1097</sup>  
 1085 Applied Probability (Taylor & Francis, 1990).<sup>1098</sup>
- 1086 [54] D. Servén, C. Brummitt, and H. Abedi, dswhah/pygam<sup>1099</sup>  
 1087 v0.8.0 (2018).<sup>1100</sup>
- 1088 [55] S. Leray, D. Mancusi, P. Kaitaniemi, J. C. David<sup>1101</sup>  
 1089 A. Boudard, B. Braunn, and J. Cugnon, Journal of<sup>1102</sup>  
 1090 Physics: Conference Series **420**, 012065 (2013).<sup>1103</sup>
- 1091
- [56] D. Wright and M. Kelsey, Nucl. Instrum. Methods A **804**, 175 (2015).
- [57] A. Kelic, M. V. Ricciardi, and K.-H. Schmidt, Abla07 - towards a complete description of the decay channels of a nuclear system from spontaneous fission to multifragmentation (2009), arXiv:0906.4193 [nucl-th].
- [58] J. Quesada Molina *et al.*, Progress in Nuclear Science and Technology **2**, 936 (2011).
- [59] M. Smy, in *International Cosmic Ray Conference*, International Cosmic Ray Conference, Vol. 5 (2008) pp. 1279–1282.
- [60] A. Ershova *et al.*, Phys. Rev. D **106**, 032009 (2022).